Aalto University

NTNU

Cold Climate Engineering

CFD Simulation of the Air Flow Field around a Ship

Aalto University Department of Mechanical Engineering
NTNU Department of Civil and Environmental Engineering

Master's Thesis

Stephan van Reen

UNIS
The University Centre in Svalbard

Nordic Master in Cold Climate Engineering

Supervisors:
Marius Jonassen (UNIS)
Richard Hann (NTNU)
Knut Høyland (NTNU)
Ville Vuorinen (Aalto University)

Abstract

This Master's thesis covers a project that aims to evaluate the effect of flow distortion on a wind sensor attached to the fjord cruise ship MS Bard using computational fluid dynamics. The simulations were performed with the Spalart-Allmaras turbulence model in steady-state. The incoming wind was modelled with a power law wind profile, and the horizontal wind angles ranged from 0° to 180°. The wind speed at the sensor height varied from 5 m/s to 30 m/s. The simulation method was validated by using it to recreate the results of a wind tunnel experiment performed on the Simple Frigate Ship Shape 2. The final simulation results indicated that the flow field around the wind sensor was generally simple, as the streamlines showed little sign of flow separation or turbulence. Furthermore, the flow around the wind sensor was found to be independent of the Reynold's number. However, no relation between the flow fields at different wind wind angles was found. Furthermore, a linear relation between the predicted wind direction and the true wind direction was found. The study also concluded that the flow field predicted by different RANS turbulence models is similar on the windward side of MS Bard, but the turbulent structures on the leeward side can be quite different. At the end of the project, a correction factor was developed with which the wind speed and direction measured by the sensor could be corrected to retrieve the true incoming wind. It was impossible to estimate the correction method's accuracy because there was no experimental data to compare.

Acknowledgements

This Master's thesis was written as part of the Nordic Master in Cold Climate Engineering. It was executed at the University Centre in Svalbard, under the supervision of the Department of Civil and Environmental Engineering at NTNU and the Department of Mechanical Engineering at Aalto University.

Firstly, I would like to thank the coordinators of the Cold Climate Engineering program Knut Høyland, Gunvor Kirkelund and Jukka Tuhkuri, for the opportunity to study at NTNU and Aalto University, and to experience a fascinating place like Svalbard.

Furthermore, I would like to thank both my supervisors Richard Hann and Ville Vuorinen for their guidance in this project. I would also like to acknowledge my UNIS supervisor Marius Jonassen for the opportunity to write my thesis at UNIS and his student Lukas Frank for assessing my Master's thesis. Moreover, I want to thank my fellow students Charlotte Gausa an Agnes Stenlund for their help in the acquisition of the necessary environmental data.

Finally, I would like to thank my family and friends for supporting me through my journey in higher education, without whom I would have never been able to get where I am today.

Stephan van Reen, Venlo, Netherlands.
28/09/2022.

Contents

List of Tables

List of Figures

Nomenclature

Abbreviations

CAD	Computer Aided Design
CFD	Computational Fluid Dynamics
DES	Detached Eddy Simulation
SA	Spalart-Allmaras (turbulence model)
SFS2	Simple Frigate Shape 2
VOS	Voluntary Observing Ship program

Naval Terminology

Bow	Front end of a ship
Centreline	Longitudinal line of symmetry of a ship
Downwind	On the side towards which the wind flows.
Green wind	Wind coming from starboard side
Port side	Left-hand side of a ship when looking towards the bow
Red wind	Wind coming from port side
Starboard side	Right-hand side of a ship when looking towards the bow
Stern	Back end of a ship
Superstructure	Structure a ship that extend from the main deck
Upwind	On the side from which the wind comes.

Symbols

α	Atmospheric stability constant (-)
$\boldsymbol{g}$	Body force per unit mass vector $(\mathrm{m/s^2})$
$\boldsymbol{u}$	Velocity vector $(\mathrm{m/s})$
ϵ	Turbulent kinetic energy dissipation rate $(\mathrm{J/(kg \cdot s)})$
μ	Dynamic viscosity $(\mathrm{kg/(m \cdot s)})$
ν	Kinematic viscosity $(\mathrm{m^2/s})$

ω	Specific turbulent kinetic energy dissipation rate $(1/\mathrm{s})$
ρ	Density $(\mathrm{kg}/\mathrm{m}^3)$
θ	Horizontal incidence angle $(^\circ)$
b	Ship beam (m)
C_{mag}	Magnitude coefficient (-)
k	Turbulent kinetic energy (J/kg)
L	Overall ship length (m)
l	Characteristic length (m)
N	Total number of cells in mesh (-)
p	Pressure (Pa)
Re	Reynold's number (-)
t	Time (s)
U	Wind speed (m/s)
u	Velocity component in the x direction (m/s)
U_{ref}	Wind speed at reference height z_{ref} (m/s)
v	Velocity component in the y direction (m/s)
w	Velocity component in the z direction (m/s)
z	Height (m)
z_0	Roughness length (m)
z_{ref}	Reference height (m)

Chapter 1

Introduction

Over the last few decades, the Arctic archipelago of Svalbard has attracted an increasing number of people, be it in the form of tourism, scientific fieldwork, or resource exploitation. All these activities rely on the weather to conduct safely, requiring accurate forecasts. However, weather prediction in the Arctic is difficult [1], and inaccuracies can have dangerous consequences. Central to much of the activity on Svalbard is Isfjorden, one of the largest fjords in Norway, which connects the settlements of Barentsburg, Pyramiden and Longyearbyen to the Arctic Ocean. In order to improve the accuracy of weather prediction in this area, the University Centre on Svalbard (UNIS) established the "Isfjorden weather information network", or Iwin project [1]. This project aims to create a high-resolution automatic meteorological measurement network by installing weather stations across Isfjorden. This includes several mobile weather stations that are installed on fjord cruise ships in the area.

These mobile weather stations are used for sea surface weather measurements, which naturally play a significant role in a water-dominated area such as Isfjorden. Two of the atmospheric properties that the weather stations measure are wind speed and direction. Performing ship-borne wind measurements is complicated by the effects of flow distortion. This phenomenon occurs because the ship's geometry affects the flow field near the sensor. This can lead to the observation of a wind vector that deviates from the unobstructed wind [2].

Figure 1.1: Map of Svalbard marking Isfjorden. From TopoSvalbard.

One of the fjord cruise ships that carries a mobile weather station on its roof as it sails tourists around Isfjorden is MS Bard, owned by Hurtigruten Svalbard AS [3]. The ship is a catamaran with many windows to give tourists a panoramic view of the fjord. The purpose of this Master's thesis is to investigate the flow distortion induced by MS Bard to develop a correction factor for the measured wind vector. This was achieved by performing computational fluid simulations on a simplified CAD model of the ship with the CFD software Ansys Fluent version 2022 R2.

This Master's thesis starts with an introduction to computational fluid dynamics in Chapter 2, followed by a literature study on the aerodynamics of ships and ship-borne wind measurements in Chapter 3. Next, Chapter 4 describes the research method, starting with a description of the validation process, which was performed using the Simple Frigate Shape 2 model developed by The Technical Co-operative Program [4]. This is a col-

laboration between the UK, USA, Canada, Australia and New Zealand on science and technology [5]. The second section of this chapter discusses the procedure for the flow distortion simulations on MS Bard. Chapter 5 presents the results of the MS Bard simulations and discusses the final correction method. This is followed by Chapter 6, which provides a critical discussion of the results and the assumptions made. Finally, the thesis is concluded in Chapter 7, which summarises the project and offers recommendations for future studies.

Figure 1.2: The hybrid-electric catamaran MS Bard on which the wind sensor is placed. From Hurtigruten Svalbard AS [3].

Chapter 2

Introduction to Computational Fluid Dynamics

This chapter provides the theoretical background in the field of fluid dynamics and CFD that is required to understand this Master's thesis. The chapter starts with an introduction to the equations that govern fluid dynamics, followed by a description of the Reynold's number. After that, turbulence modelling and turbulent boundary layers are discussed. Finally, the chapter concludes with a description of the boundary conditions that were employed in the simulations and an explanation of wind profiles.

2.1 Navier-Stokes Equation

The motion of a Newtonian fluid like air is modelled using the Navier-Stokes equation, which represents the momentum balance within a system. Any change in the momentum of the fluid flow must correspond to a force acting on this fluid. Kundu and Cohen [6] give the vector form of the Navier-Stokes equation for incompressible flows as Equation 2.1. In incompressible flows, the density of the fluid does not change with pressure and is considered constant. [6]

$$\rho[\frac{\partial \boldsymbol{u}}{\partial t} + (\boldsymbol{u} \cdot \boldsymbol{\nabla})\boldsymbol{u}] = -\boldsymbol{\nabla} p + \rho \boldsymbol{g} + \mu \nabla^2 \boldsymbol{u}. \tag{2.1}$$

The left-hand side of the equation corresponds to the change in momentum of the fluid and contains the velocity vector $\boldsymbol{u}$, the time t, and the fluid density ρ. The first term represents the change in momentum with time. The second term is the convective acceleration, representing the transport of a fluid property, in this case, the momentum, by the ordered motion of the flow. [6]

The right-hand side of Equation 2.1 consists of the forces that induce the change in momentum. p is the mechanical pressure applied to the flow at its boundaries. Thermodynamic pressure, which is the pressure within a fluid that results from temperature and volume changes, is not defined for incompressible flows. Moreover, the incompressible Navier-Stokes equation only involves pressure gradients, not absolute pressures. [6]

The variable $\boldsymbol{g}$ is the body force per unit mass vector. A body force is a force that is applied throughout the entire fluid mass by a force field. Examples of body forces are gravity and electrostatic force. μ is the dynamic viscosity, which is the property of a fluid that relates the shear stresses applied to the fluid to its deformation rate. [6]

The first term on the right-hand side of Equation 2.1 is called the pressure term, which corresponds to the normal forces induced at the fluid boundaries by the mechanical pressure [6]. The second term represents the body forces acting on the fluid [6]. Finally, the last term is the viscous force term. Viscous forces oppose the relative motion of adjacent fluid layers, analogous to the friction between two solid surfaces [7]. However, unlike the friction between solids, viscous forces increase with relative speed [7].

2.2 Continuity Equation

In the same way that the Navier-Stokes equation describes the conservation of momentum in the flow, the conservation of mass in the flow is described using the continuity equation. Any physical solution to the Navier-Stokes equation must also obey the continuity equation. For incompressible flows, the continuity equation is: [6]

$$\boldsymbol{\nabla} \cdot \boldsymbol{u} = 0, \tag{2.2}$$

where all the variables are the same as in Equation 2.1. In a physical sense, the incompressible continuity equation states that the total volume of a region of fluid is constant. Thus, if the fluid region changes in one dimension, this change must be compensated by a change in the other dimensions.

2.3 Reynold's Number

The Reynold's number Re is a similarity parameter that represents the influence of viscosity on a flow case relative to the influence of inertial forces [6]. The Reynold's number is often expressed in the context of the flow through a pipe or over an object. The equation for the Re is: [6]

$$Re = \frac{\rho U l}{\mu} = \frac{U l}{\nu}, \tag{2.3}$$

where U is the incoming flow speed, and ν is the kinematic viscosity. The symbol l is the characteristic length, which is a dimension of the object that is representative of the scale

of that object. For the flow in a pipe, l is often the diameter [8], while in the case of the airflow around a ship, l is usually either the length [9] or the beam [4]. In this project, the value for l will be equal to the distance the wind travels over the ship, e.g. for headwind, this is the ship's length, for a 90° wind, it is the ship's width, and for a 45° wind it is the diagonal length of the ship.

When two flow cases over an identical shape and with identical boundary conditions have the same Reynold's number, they will have the same non-dimensional solution, regardless of scale [6]. As a result, the non-dimensional flow field around an object in a model scale experiment is approximately identical to that of the full-scale object in the same conditions.

2.4 Turbulence and RANS

Like most flows in nature, wind is generally turbulent. Turbulent flows are non-linear, dissipative, random and vortical [6]. Small perturbations lead to large changes, constantly causing the flow structure to change. The flow is very chaotic and can require a vast amount of time to simulate. However, even turbulent flows have some gross characteristics, such as the mean velocity, that can be modelled with more modest computing power by solving modified Navier-Stokes equations. [6]

One of the simplest methods to solve the Navier-Stokes equations for turbulent flows is using Reynolds decomposition. In this method, the flow variables, like velocity u and pressure p, are split into a mean, and a fluctuating component, the latter representing the deviation of the flow variable from the mean [6]. By applying Reynolds decomposition to every variable in Equation 2.1 and averaging all the terms, the Reynold's Averaged Navier-Stokes equation, or RANS equation, is found [10]:

$$\rho\frac{\partial\bar{u}_i}{\partial t}+\rho\bar{u}_j\frac{\partial\bar{u}_i}{\partial x_j}=\rho g_i-\frac{\partial\bar{p}}{\partial x_i}+\frac{\partial}{\partial x_j}(\mu(\frac{\partial\bar{u}_i}{\partial x_j}+\frac{\partial\bar{u}_j}{\partial x_i})-\rho\overline{u_i'u_j'}). \tag{2.4}$$

Note that this equation is written in tensor form. The variable u' is the fluctuating component of the velocity vector, and any variable with a bar over it is an averaged variable. The process of decomposition and averaging has led to the creation of an additional term $\rho\overline{u_i'u_j'}$, known as the Reynolds stress [10]. This term can be interpreted as the rate of mean momentum transfer by turbulent fluctuations [6]. The Reynold's stress is a fourth unknown, next to the velocity components that the Navier-Stokes equation already solves. Thus, this variable must be approximated, or one or more extra equations must be added to solve the RANS equation [6]. Methods to solve for Reynold's stress are called closures [6].

2.5 Turbulent Boundary Layer and y+

When a fluid flow encounters a wall, the speed of the fluid layer in direct contact with the wall will decrease to zero. The speed of the fluid then increases with distance from the wall until the free-stream speed is reached. This area of decelerated flow is called a boundary

layer. The boundary layer of a turbulent flow is governed by the Law of the Wall, which says that the non-dimensional velocity profile in a turbulent boundary layer is a function of the dimensionless distance from the wall $y+$. A turbulent boundary layer is generally split up in 3 main layers, drawn in Figure 2.1. [6]

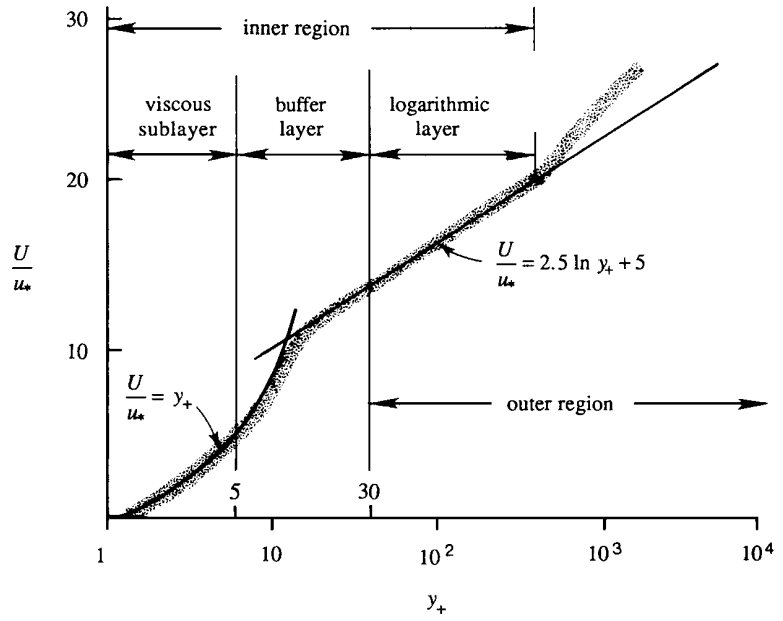

Figure 2.1: Turbulent boundary layer split into three main layers: the viscous sub-layer, the buffer layer and the logarithmic layer. From: Kundu and Cohen [6].

As its name suggests, the viscous sublayer is dominated by viscous effects. The logarithmic layer, also referred to as the inertial sublayer, is a region where viscosity has little influence. The buffer layer is the transition layer between the viscous and inertial sublayers. [6]

When performing CFD, the height of the first layer of cells above a wall determines how much detail of the boundary layer can be simulated. This height is determined using the $y+$ value. For example, if the $y+$ value of the first cell layer is greater than 5, the entire viscous sublayer is reduced to one layer of cells, and thus its detailed structure is lost. The minimum cell height to achieve a specific $y+$ value can be determined by a set of equations based on the Blasius solution for a flat plate boundary layer [11].

2.6 Turbulence Models

There are many ways to model turbulence in CFD, each requiring varying amounts of computing power. At the low end of this spectrum lie the RANS turbulence models that aim to solve the previously discussed RANS equation (Equation 2.4). A more compu-

tationally expensive method is Large Eddy Simulation (LES) which directly solves the Navier-Stokes equations for large-scale turbulent flow structures but merely approximates the effect of smaller structures [10]. At the top of the spectrum lies Direct Numerical Simulation (DNS), which is used to directly solve all turbulent structures at any scale [10]. This method is much more computationally expensive than LES [10].

Since both LES and DNS are much more computationally expensive than RANS turbulence models, their use is limited in smaller projects. RANS models are generally suitable for the simulation of attached turbulent flows, but cannot reliable simulate turbulent structures due to the averaging procedure behind the RANS equation [10]. Among the most commonly used RANS turbulence models are the two equation k-ε, k-ω, and k-ω SST models and the one-equation Spalart-Allmaras model.

2.6.1 Turbulence Model: k-ε

The k-ε turbulence model is a well-known model that seeks to close the RANS equation by solving two extra transport equations: one for the turbulent kinetic energy k, and one for the rate of turbulent kinetic energy dissipation ϵ [12, 10]. This turbulence model is suitable for free-shear-layer flows and wall-bounded flows with a small or zero adverse pressure gradient [12]. However, the model is less accurate for flows with a large adverse pressure gradient [12]. Furthermore, a fine grid near the wall, as well as additional so-called wall damping functions, are required to resolve the viscous sub-layer [12, 10]. Lastly, the k-ε model under-predicts the deceleration of boundary layer flow in an adverse pressure gradient, which in turn delays separation [12].

2.6.2 Turbulence Model: k-ω

The k-ω turbulence model is similar to the k-ε model in that it closes the RANS equation by solving two transport equations, including the one for k [12]. But instead of the equation for ϵ, this model solves a transport equation for ω, which is the specific turbulent kinetic energy dissipation rate [12]. The k-ω model does not require wall damping functions to resolve the viscous sub-layer [12], and is more accurate than the k-ε model for a logarithmic layer with an adverse pressure gradient [12]. The downside of this model is that it is highly sensitive to the value of ω in the free-stream, making it less accurate for free-shear-layer flows [10, 12], and on the edge of a boundary layer [10]. Furthermore, like the k-ε model, the k-ω model does not accurately predict separation in adverse pressure gradients [12].

2.6.3 Turbulence Model: k-ω SST

The k-ω SST model was created as an attempt to combine the good aspects of the k-ε and k-ω models into one turbulence model [10]. This combined model switches between the k-ε and k-ω models, depending on a cell's distance to the wall. It utilises the k-ω model within the inner 50% of the boundary layer [13], which includes the viscous sub-layer and logarithmic layer [10]. As the distance to the wall increases further, the k-ω SST model gradually transforms into the k-ε model [13]. The k-ε model is also applied for

free-shear-layer flows, leading to almost identical results for such flow cases [13]. The k-ω SST model is accurate for boundary layer flows with an adverse pressure gradient and unlike k-ω does not depend on the free-stream value of ω [13]. It also accurately predicts backwards-facing step flows, even though the normal k-ω model performs better in this case [13]. Lastly, the combined model more accurately predicts flow separation in adverse pressure gradients than its constituents [12].

2.6.4 Turbulence Model: Spalart-Allmaras

The Spalart-Allmaras turbulence model (here referred to as the SA turbulence model) was developed to predict aerodynamic flows in the aerospace industry, by employing a single extra transport equation for the turbulent viscosity [12]. The use of a single equation generally makes computations with the SA model faster than with two-equation models [14]. Furthermore, the SA model does not require a high cell resolution to properly model near wall flow [10, 12]. This model provides more accurate results for adverse pressure gradient flows than either the k-ε or k-ω models, but it is still less accurate than the k-ω SST model [12, 10]. Moreover, it does not accurately model jet flows [12].

2.7 Boundary Conditions

Boundary conditions act as the inputs and limitations to a flow case, which allow the case to be solved. Though many different boundary conditions exist, only the ones used in this project will be discussed in this section. Note that different solvers may apply different names to the same boundary condition. Thus, to avoid confusion, the names used by Ansys Fluent will be used exclusively. More detailed information about each boundary condition can be found in the Ansys Fluent User's Guide [15].

2.7.1 Velocity Inlet and Pressure Outlet

Inlet and outlet boundary conditions determine the location where the flow enters and leaves the computational domain, as well as the flow properties at these locations. The velocity inlet is an inlet condition that defines the incoming flow velocity vector [15]. It also allows for the specification of scalar flow properties, such as temperature, turbulence parameters, and gauge pressure. The gauge pressure is an important scalar property for density-based solvers. For pressure-based solvers, the gauge pressure can be left as zero. [15]

The pressure outlet condition defines the static pressure at the domain exit [15]. The specified static pressure will affect the upstream flow conditions, which in turn determine the outlet's dynamic pressure. The static pressure can be set to zero to simulate the free-stream condition.

2.7.2 Symmetry

A symmetry boundary condition is used to define a plane of symmetry. The gradient of any variable normal to the symmetry plane is zero [15]. Likewise, the velocity component

normal to the boundary is also zero, which means that the velocity vector at the symmetry boundary condition will always be parallel to the symmetry plane. The symmetry boundary condition can be used as a zero-shear slip wall in viscous flows [15].

2.7.3 Wall Condition

There are two kinds of wall conditions that are commonly used in CFD: no-slip wall and specified shear [15]. A no-slip wall is normally used as the boundary between the fluid and a solid object. No-slip means that the flow velocity vector relative to the boundary equals zero at the boundary [10]. The velocity increases with distance from the wall until it equals the velocity of the free-stream, creating a boundary layer.

The specified shear wall boundary condition allows for the specification of a shear force applied to the fluid at the wall [15]. If the applied shear force vector is equal to zero, the velocity at the boundary will be equal to the free-stream velocity. Yuan et al. [4] refer to this kind of wall condition as a slip wall. If the applied shear force is greater than zero, the velocity at the boundary will be smaller than the free-stream velocity.

2.7.4 Wind Profile

The velocity of wind varies with height, which can be described with a 2D wind profile [16]. These 2D wind profiles are often approximated mathematically with one of the following expressions: a power law approximation or a logarithmic approximation [16]. The simplest of these two expressions is the power law approximation, which is commonly used in ship airflow studies, including the papers by Forrest and Owen [17] and Wang et al. [18]. The power law-based wind profile is expressed as follows [16]:

$$U = U_{ref}(\frac{z}{z_{ref}})^{\alpha}, \tag{2.5}$$

where U is the velocity calculated at a certain height z, z_{ref} is the reference height and U_{ref} is the wind speed at this reference height [17]. α is an empirical constant that depends on atmospheric stability [19].

The logarithmic wind profile is generally more accurate than the power law profile within the surface layer of the atmospheric boundary layer [16]. The atmospheric boundary layer is the lowest part of the atmosphere and is influenced by the ground [16]. The surface layer is, in turn, the lowest part of the atmospheric boundary layer [16]. Its height increases with wind speed, and the surface layer can be as high as hundreds of metres [16]. The power law gives a better approximation of the wind profile above the surface layer [16]. The formula for a logarithmic wind profile is shown in Equation 2.6 [16], where z_0 is the roughness length, which is an empirical constant that depends on the roughness of the terrain.

$$U = U_{ref}\frac{\ln(\frac{z}{z_{ref}})}{\ln(\frac{z}{z_0})} \tag{2.6}$$

Chapter 3

Literature Study

In the past, research on the fluid dynamics of a ship has primarily focused on hydrodynamics [9]. The use of fluid dynamics in marine engineering was often limited to evaluating resistance and loading, and water generally induces much higher forces than air. Thus, the study of aerodynamics was limited to the design of sailing vessels. However, with the encroaching threat of climate change and government regulations, ship owners are looking into all sorts of ways to decrease the fuel consumption of their vessels. Ships with extensive superstructures, such as cruise ships and container vessels, can experience significant amounts of drag from the air and thus see significant benefits from an aerodynamic design [18]. Additionally, as the use of helicopters on naval craft became commonplace, research started on the turbulent air in the vicinity of the helipad [9, 20]. Thus, the aerodynamics of ships has become an important research topic in recent decades [9].

Parallel to these developments, more and more ships have been equipped with wind sensors, the data from which is not only used by the ships themselves but also for weather prediction and meteorological research [2]. Besides research ships, many commercial ships have voluntarily installed such wind sensors as well [2]. However, ship-borne wind measurements do not necessarily provide a correct picture of the undisturbed wind [2]. This is because the ship distorts the airflow around it and thus influences the wind measurements. Therefore, in the past couple of decades, the results of aerodynamic research, computational fluid dynamics (CFD) and model experiments have been used to correct this influence and improve measurement accuracy [2].

3.1 Aerodynamics of a Ship

This section discusses previous scientific studies on the aerodynamics of examples of three different ship types: military frigates with a helipad [17, 21, 4], cruise ships [18] and megayachts [9].

3.1.1 Aerodynamics of the Simple Frigate Shape 2

The usage of helicopters in ship-borne military and civilian operations created a requirement to understand the influence of the superstructure's wake on take-off and landing operations [20]. Computational Fluid Dynamics was essential to modelling this wake, and so The Technical Co-operative Program created the Simple Frigate Shape 2 (SFS2) to be used as a benchmark for the validation of CFD codes. A drawing of the SFS2 is shown in Figure 3.1.

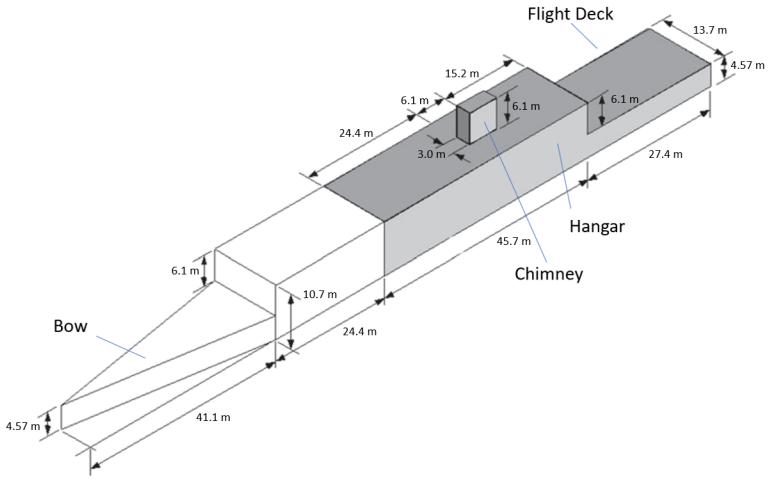

Figure 3.1: Drawing of SFS2, including dimensions in metres. From: Yuan et al. [4].

Forrest and Owen [17] analysed the flow around this model at wind angles of 0°, 45° and 90°, using unsteady Detached Eddy Simulation (DES) and a wind speed of 25.7 m/s. In order to represent a natural wind, a wind profile was introduced in the form of a power law, with an α value of 0.13. The paper contained little information about the 90° results.

At a 0° wind angle, also referred to as headwind, the flow separated from the top and side edges of the SFS2 superstructure, leading to the formation of turbulent eddies that travel downstream. The separated flow then re-attached further downstream before separating again from the side and top edges at the end of the superstructure. These final separations then generated a 3D re-circulation bubble in the lee of the superstructure. This was also observed by Kääriä et al. [21], who performed effectively the same analysis on the SFS2 model but at a different wind speed of 20.6 m/s. They also observed that the separation area has a significant downward component and that the flow does re-attach aft of it

[21]. Moreover, another separation bubble forms behind the stern of the ship [21]. Lastly, Forrest and Owen [17] observed that while the mean behaviour of the headwind flow is symmetric about the longitudinal axis, the instantaneous behaviour is not, while Kääriä et al. [21] concluded that the turbulent behaviour was also reasonably symmetrical.

The simulation was repeated with the wind at a 45° wind angle from the starboard side, which in naval terminology is called green 45° wind. Here Forrest and Owen [17] observed the formation of a diagonal vortex at the starboard edge of the superstructure that flowed towards the port side, as shown in Figure 3.2. Furthermore, a lateral vortex formed on the front edge of the superstructure.

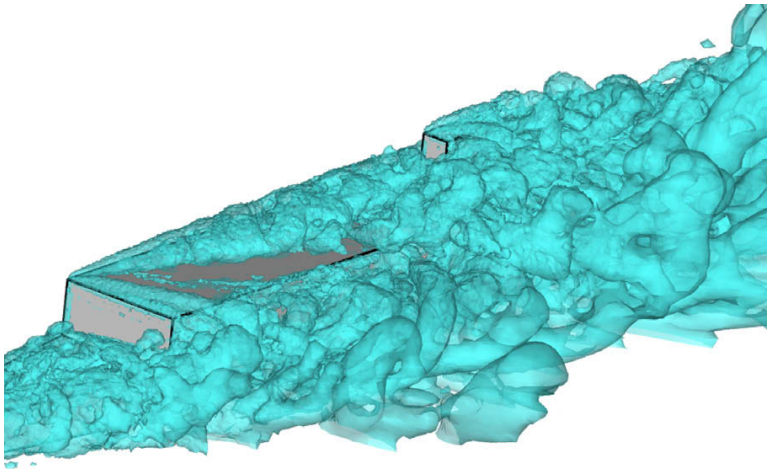

Figure 3.2: Flow structures at the front of the SFS2 superstructure at a 45° wind angle towards the windward side. From: Forrest and Owen [17].

Figure 3.3 shows the flow at the stern of the SFS2 [17]. At the horizontal edge at the back of the superstructure, the vortex flowing over the top of the structure begins to break down and shed helical vortices over the helipad (structure c). Moreover, the flow along the starboard face of the superstructure separates from the vertical aft edge, forming a flapping shear layer (structure b). Finally, a vortex forms as the free stream over the aft of the ship mixes with the longitudinal flow travelling along the starboard side of the hull (structure a). Kääriä et al. [21] observed similar behaviour at a green 30° wind angle. A large amount of turbulence over the helipad was caused by the shear layer separating from the top edge of the superstructure, as well as the flapping shear layer at the starboard vertical edge.

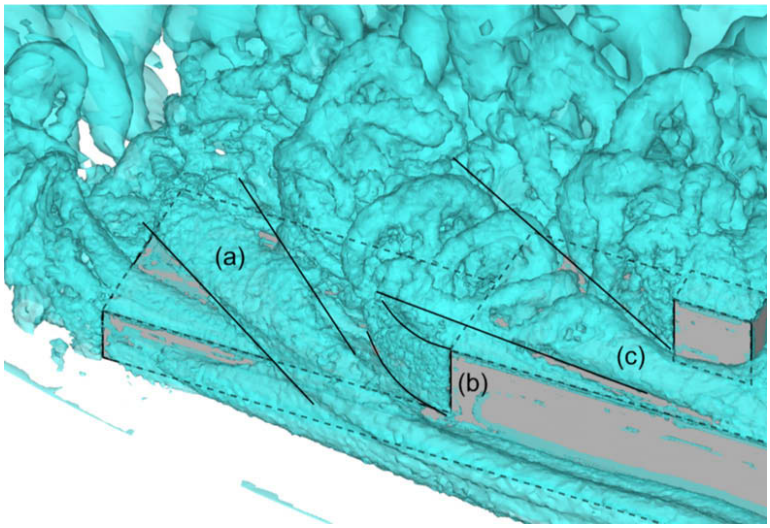

Figure 3.3: The wake aft of the SFS2 model superstructure at a 45° wind angle towards the windward side. From: Forrest and Owen [17].

Yuan et al. [4] used the open-source CFD software OpenFOAM to simulate the air wake of the Canadian Patrol Frigate (CPF) for use in helicopter flight simulators. In order to determine if OpenFOAM would be suitable for ship air wake simulations, the software was validated by performing a CFD simulation on the SFS2 and comparing it with results from a wind tunnel experiment on a SFS2 model.

The experiment was performed with a 1:100 scale model, subjected to wind at two different angles: headwind (0°) and green 45°. The Reynold's number used for each test was $5.4e5$ for headwind and $4.5e5$ for green 45° wind, with wind speeds of 60 m/s and 50 m/s, respectively. Hot film anemometry was used to measure the velocity profile on four vertical planes, located at 0%, 25%, 50%, and 75%, the length of the flight deck. In the headwind case, these planes are called Map 1a, Map 1b, Map 1c and Map 1d, respectively, and are shown in Figure 3.4. For the green 45°wind, the planes are called Map 3a, Map 3b, Map 3c and Map 3d. [4]

The CFD simulations of the SFS2 were also performed on a 1:100 scale Computer-Aided Design, or CAD model. A structured grid was used to improve grid quality, consisting of about six million cells. The turbulence was modelled with a Spalart-Allmaras delayed Detached Eddy Simulation. Slip boundary conditions were used for both the top boundary and the water surface, and a no-slip boundary condition was applied to the CAD model. The Reynold's numbers were the same as in the experiment. [4]

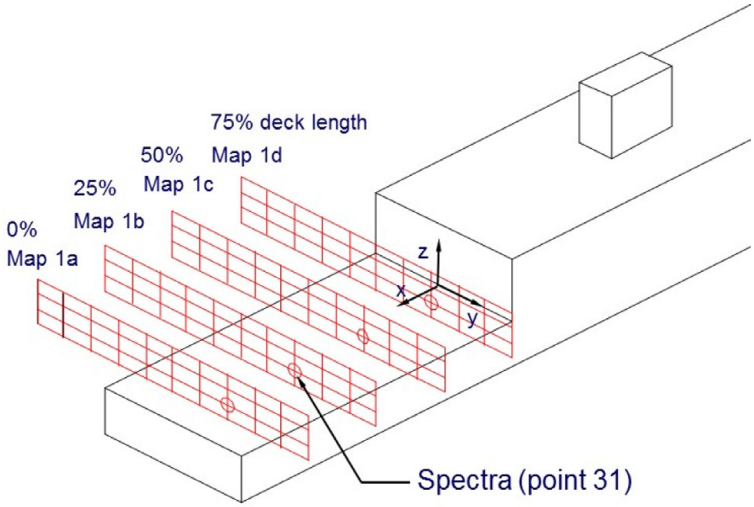

Figure 3.4: Locations of the hot film anemometry measurement planes used in wind tunnel tests. Locations are given as percentage of flight deck length. From: Yuan et al. [4].

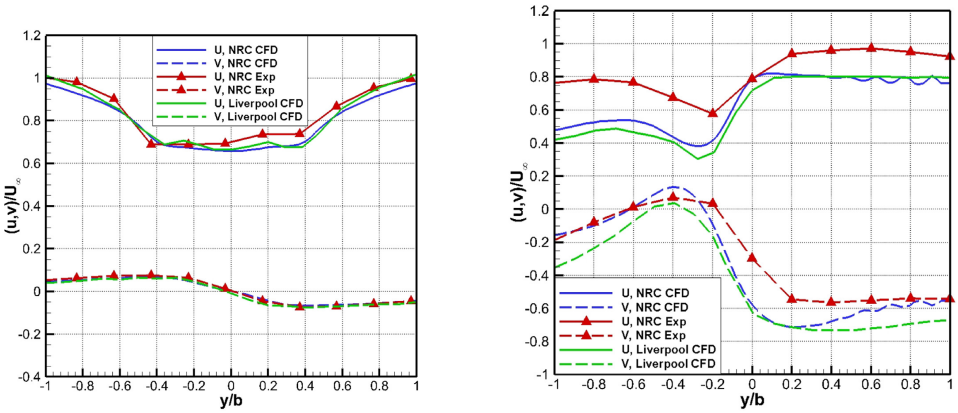

(a) Map 1c, headwind.

(b) Map 3c, Green 45° wind.

Figure 3.5: Velocity profiles on Map 1c and Map 3c at hangar roof height. Includes the experimental and simulation data from Yuan et al. [4] (NRC) and the simulation data from Forrest and Owen [17] (Liverpool). From: Yuan et al. [4].

The resulting velocity profiles at Map 1c and 3c (headwind and green 45° wind) are shown in Figure 3.5. The profiles are from the height of the hangar roof. The red curves with triangular markers show the experimental data. The blue curves, called NRC CFD, are the simulation results from the currently discussed study by Yuan et al. [4]. Finally, the green curves, called Liverpool CFD, are the results from the previously discussed study by Forrest and Owen [17], determined at the same position as Map 1c and 3c.

In both plots, the horizontal axis is the lateral position y, normalised by the ship beam b. Thus, the full width of the ship lies between $y/b = -0.5$ and $y/b = 0.5$. The figure shows strong agreement between both simulations and the experiment for the Headwind case. A notable difference is that the longitudinal velocity u measured in the experiment is asymmetric about the ship centreline, while the simulation results are not. The paper does not discuss this asymmetry further. Nevertheless, the maximum discrepancy between the NRC CFD results and the experiment is only roughly 3%. Furthermore, the headwind plot shows that the longitudinal velocity is reduced within the wake of the hangar and increases sharply when $|y/b| > 0.4$. On the other hand, the lateral velocity v stays relatively constant until it switches direction around the centreline.

In the green 45° case, the agreement between the simulations and the experiment is not as good, only showing qualitative agreement. Yuan et al. [4] believe that the differences observed between the simulations and the experimental data result from some anemometer films being located in the wake of other films at the green 45° wind angle. Moreover, both simulations show similar results, with the NRC flow field corresponding with the Liverpool flow field in Figure 3.3, characterised by separated flows and a vortical structure coming from the edges of the hangar [4, 17].

Su and Xu [22] investigated the coupled flow field of a ship and a helicopter rotor. They used the data from Yuan et al. [4] to validate their CFD simulation on the SFS2. They employed the unsteady density based Navier-Stokes solver from Ansys Fluent, and for closure, they used the k-ω turbulence model. The time-averaged simulation results are compared to the experimental data in Figure 3.6.

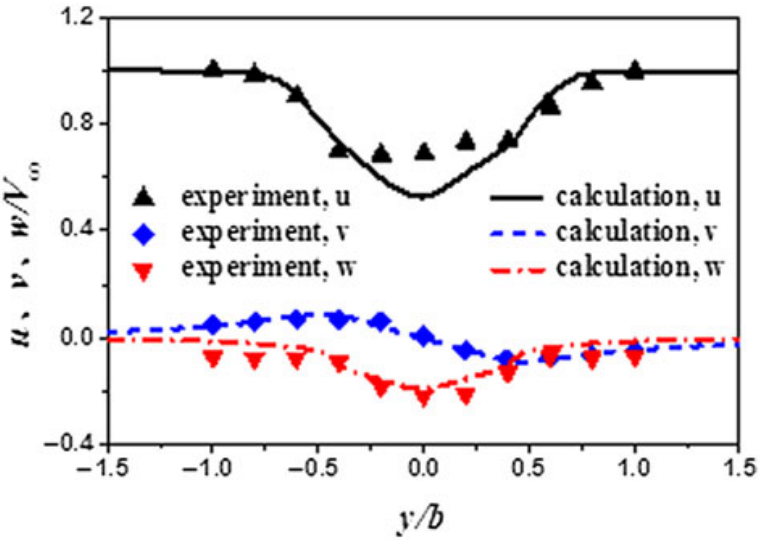

Figure 3.6: Headwind velocity profiles on Map 1c from simulations by Su and Xu [22]. includes experimental data by Yuan et al. [4]. From Su and Xu [22].

In contrast to Figure 3.5a, the simulated longitudinal velocity u is significantly smaller than the experimental data and forms a valley in this area. Furthermore, the simulated lateral velocity closely matches the experimental data, whereas the vertical velocity w shows some minor discrepancies.

3.1.2 Aerodynamics of a Vista-class cruise ship

Wang et al. [18] analysed the flow over a model scale Vista-class cruise ship, shown in Figure 3.7. The wind angle ranged from 0° to 180°, coming from the starboard direction, with 15° intervals. They compared standard empirical formulae for calculating the wind load coefficients to wind tunnel experiments and CFD simulations. The wind was modelled using a power law wind profile with $\alpha = 0.125$. The CFD simulations were also in model scale, with the computational domain made to match the wind tunnel, and a steady k-ε turbulence model was used.

The wind tunnel experiment and simulations were done at a Reynold's number of $1.28\text{e}6$. A Reynold's number independence analysis was performed to ensure that the results of this study would apply to a full-scale ship. The results showed that when Reynold's number exceeds $1.0\text{e}6$, the wind load coefficients become independent of Reynold's number, and so the results could indeed be concluded to be representative of the full-scale ship.

Figure 3.7: Scale model of Vista class cruise ship, used for the wind tunnel experiment by Wang et al. [18].

In the headwind case, the wind flowed smoothly along the external surface of the ship, symmetric about the longitudinal axis, until flow separation occurred at the end of the superstructure. This separation led to the generation of two areas of reversed flow behind the structure, which, too, were symmetric about the longitudinal axis. [18]

At wind angles between 15° and 60° there was no more symmetry about the longitudinal axis, as shown in Figure 3.8a for a 45° wind angle. The incoming flow would separate from the corners of the bow decks but would not re-attach anymore. This flow would then form into a longitudinal trailing vortex that became wider and more distinctive with increasing wind angle. Flow separation also occurred at the corners of the aft decks but without forming into a clear vortex. This separated flow structure was also smaller than the bow vortex. [18]

When the wind angle reached 75°, the bow vortex turned into a D-shaped re-circulation bubble. At 90°, shown in Figure 3.8b, the flow that had separated from the aft deck also formed a D-shaped re-circulation bubble. As the wind angle increased further, the flow came from the stern side, and the previously discussed flow patterns were effectively repeated in reversed order. At a 180° wind angle, reverse flow zones occurred at the rear of the ship, and the flow separated at the front.

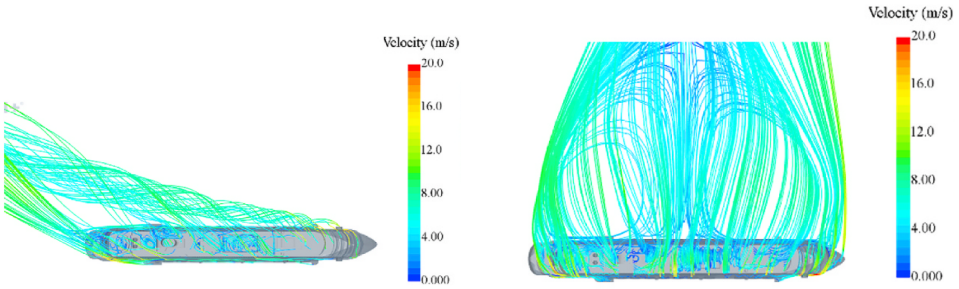

(a) 45°. **(b)** 90°.

Figure 3.8: Simulated streamlines of a Vista-class cruise ship model, at wind angles of 45° and 90°. From: Wang et al. [18].

3.1.3 Aerodynamics of a Megayachts

Similar to the previous article, Trivyza and Boulougouris [9] investigated the flow around the superstructure of a megayacht using a CFD simulation. The 3D model was designed to represent the general shape of a megayacht superstructure and is shown in Figure 3.9.

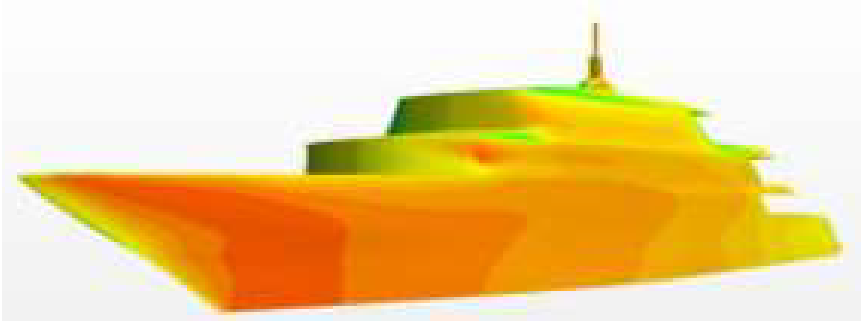

Figure 3.9: 3D model representative of megayachts used in the CFD simulation by Trivyza and Boulougouris [9].

The simulations were time-dependent and performed using a RANS k-ω SST turbulence model. The wind angle of the incoming wind varied between 0° and 90°, with intervals of

15°. The atmospheric boundary layer was not modelled, so the flow velocity at the inlet did not vary with altitude. The simulation was repeated at two different wind velocities: 2.6 m/s and 10.3 m/s. The paper only presents the results at a speed of 10.3 m/s, because the authors found no difference between the general flow characteristics at the two speeds, except for the magnitudes. [9]

The simulated flow fields are shown in Figure 3.10. In the headwind condition, the flow was symmetric about the centreline, with two primary counter-rotating vortices generated by flow separation from the front edges of the main deck. Smaller eddies arose due to trailing edge separation from the other decks, strengthening the two larger vortices. At a 15° wind angle, two strong vortices were created: one caused by flow separation from the trailing edges of the helideck and one created by flow separation at the back of the main deck. Far behind the ship, these two vortices combined into a single larger vortex. [9]

At an wind angle of 30°, the main source of vorticity was a large separation area at the front of the main deck and eddies created at the starboard sides edges of the superstructure. These sources combined to create a wide, stretched vortex at the stern side of the superstructure. For the 45° wind angle, flow separation occurred at the forward part of the superstructure. The separated flow generated a large vortex, which was also strengthened by the eddies resulting from separation at the ship's starboard side. [9]

At the final wind angle of 90°, the flow was strongly turbulent on the starboard side and fully detached from most surfaces of the vessel. The highest flow speed values were reached in this scenario, as well as the greatest turbulence and vorticity levels. Both a strong vortex and a large re-circulation area are visible coming from the bow in Figure 3.10d, and streamlines of separated flow are clearly visible at the stern. [9]

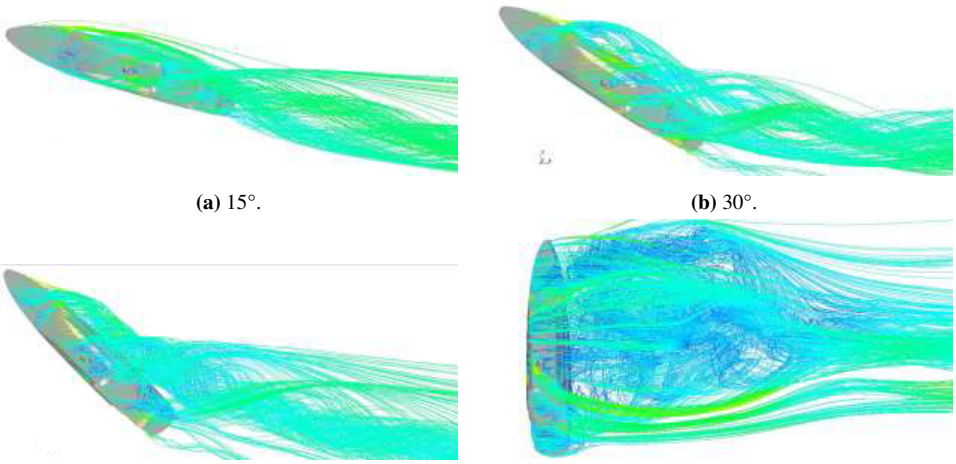

(a) 15°. **(b)** 30°. **(c)** 45°. **(d)** 90°.

Figure 3.10: Simulated streamlines of a megayacht cruise ship model, at wind angles of 15°, 30°, 45° and 90°. From Trivyza and Boulougouris [9].

3.2 Reynold's Independence

In the previous section, it was stated that Forrest and Owen [17] and Kääriä et al. [21] analysed the flow around the same SFS2 model, but at different initial wind speeds of 25.7 m/s and 20.6 m/s, respectively. This relates to the common assumption that the flow field over a bluff-body with sharp edges is independent of the Reynold's number [17], provided it exceeds a value of about $2...3e4$ [23]. This assumption is commonly applied to the superstructure of ships because it is usually made up of sharp-edged, rectangular blocks, which are bluff bodies. The physical explanation is that flow separation over a bluff body is said to always occur at sharp edges, regardless of the object's size or the flow speed [24]. Besides this, it is assumed that the flow re-attachment, which may or may not occur, is also independent of Reynold's number [24].

Reynold's number independence is important in the context of CFD simulations of wind flow distortion because a ship can be subjected to significant range of wind speeds. A change in wind speed leads to a change in Reynold's number, so if the flow field around a ship depends on Reynold's number, the simulation must be repeated at multiple different speeds to develop a suitable correction method. However, if the flow field is independent of Reynold's number, it would suffice to only simulate at a single wind speed and use a correction factor to correct for the different speeds. This would save a significant amount of computation time. Trivyza and Boulougouris [9] concluded the the latter option was valid for their project, having simulated the flow over a megayacht model at two different wind speeds, 2.6 m/s and 10.3 m/s, and finding no difference in general flow characteristics, except for the magnitudes of the physical quantities changing with speed.

However, the Reynold's number independence assumption is disputed. As previously discussed, Wang et al. [18] found that Reynold's number independence was only achieved when the Reynold's number exceeds $1.0e6$, which is two orders of magnitudes higher than the value of $2...3e4$ that is usually applied [23]. Hoxey et al. [25] compared the pressure coefficients at different positions on a full-scale sharp-edged triangular roof (Figure 3.11a) with the flow over a 1:100 model scale version. They concluded that the separated flow at the windward slope of the roof was Reynold's number dependent. However, they also repeated the experiments with a roof with rounded edges (Figure 3.11b), and found that this produced a predominantly attached flow that was independent of the Reynold's number. This last conclusion is surprising because the idea behind the Reynold's number independence of sharped edged bluff bodies rests on the expectation that the flow will always separate at a sharp edge, but in this case, there was no separation or a sharp edge.

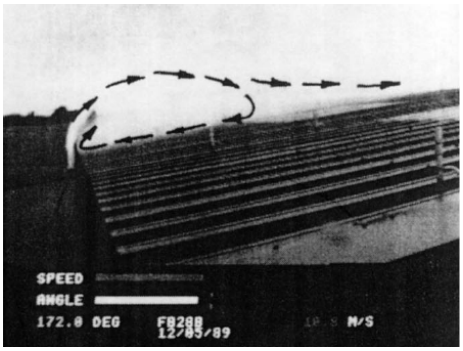

(a) Wind flow over a sharp-edged roof.

(b) Wind flow over a roof with rounded edges.

Figure 3.11: Wind flow over a triangular roof experiment, with sharp (a) and rounded edges (b). Figure adapted from Hoxey et al. [25]

The experiment by Hoxey et al. [25] and four other full-scale to model scale comparisons on bridges were reviewed by Larose and D'Auteuil [24]. They, too, concluded that the flow over sharp-edge bluff bodies could be sensitive to Reynold's number effects and recommend that the presence of these effects should be investigated before assuming independence. Furthermore, Lim et al. [23] investigated the influence of Reynold's number on a cube deeply submerged in a turbulent boundary layer. This was done by analysing the flow over a cube at two different Reynold's numbers and a much larger 6-meter high cube under natural wind conditions. They had the cube in two orientations: the flat side facing the incoming flow and at a 45° angle so that an edge faced the flow. The former case represented a scenario without strongly concentrated or relatively steady vortex regions, for which the pressure and velocity field did not significantly depend on Reynold's number. The latter case represented flow fields with strongly concentrated or steady vortices, which clearly showed a dependence on Reynold's number.

Accordingly, the presence of steady vortices observed by Forrest and Owen [17], Wang et al. [18] and Trivyza and Boulougouris [9] (as described in Section 3.1), implies that the turbulent airflow over a ship superstructure may be dependent on the Reynold's number, even if that was not the case for Trivyza and Boulougouris [9]. Thus it is recommended that the flow simulation over a ship is performed at different wind speeds unless the results show that the flow field is independent of Reynold's number after all.

3.3 Ship Flow Distortion

With an understanding of ship aerodynamics, it is possible to evaluate the effects of flow distortion by a ship on wind measurements. A correction method can then be developed to correct these measurements to reflect the real wind conditions accurately. These methods are created using CFD because, unlike in the real world, the initial wind conditions are known precisely as the user specifies them.

Most studies in flow distortion are performed on research ships, such as the research vessels Oden [26] and RV Knorr [27]. However, despite several thousands of merchant vessels being outfitted with wind sensors as part of the Voluntary Observing Ship program (VOS), very little research has been performed on the flow distortion of merchant vessels [2]. This is because the large variety in shape and size of these vessels makes it difficult to say anything about them as a group, and the sheer number of ships makes studying each individual ship unfeasible [2]. In this section, the flow distortion studies on Oden [26] and RV Knorr [27] are discussed.

3.3.1 Flow Distortion by the Icebreaking Vessel Oden

In 2014, the icebreaking research vessel Oden was outfitted with two sonic anemometers as part of the ASCE[1] programme [26]. These two anemometers were placed above one another at the ship's bow, on the centreline. The ship also had two anemometers of its own and a weather station on the bridge, as well as a lidar and an aerosol intake on its superstructure. The sensor locations are shown in Figure 3.12. [26]

The flow distortion at these locations was investigated by Moat et al. [26], using the Reynold's Average Navier Stokes (RANS) solver VECTIS. The flow was modelled as steady-state, and the k-ε turbulence model was employed. The direction of the incoming wind varied between 0° (headwind) and 120° at 10° intervals. Furthermore, an additional run was performed at 150°. The atmospheric boundary layer was modelled using a logarithmic profile with a 10 m speed of 7 m/s and a Von Karman constant of 0.4.

In a headwind, the top bow anemometer saw a 3% wind speed deceleration, which increased to a 12% acceleration as the wind angle increased to 120°. Similarly, the bottom bow anemometer experienced a 5.5% deceleration in headwind wind and a 16% acceleration at 120°. The streamlines were displaced vertically by 3 m w.r.t. their starting height in the headwind case and 6 m for the 90° wind.

The ship's own anemometers experienced a 2% to 10% acceleration in flow speed over the range of incoming horizontal wind angles. Conversely, the flow speed at the weather station tended to decrease severely for angles greater than 70°. At this angle, the weather station was in the shadow of the ship structure. The vertical displacement of the streamlines at the weather station ranged from 11 m at 10° to 24 m at 110°.

[1] ASCE stands for the Adapting to Climate Change and Sustainable Energy programme by the EU.

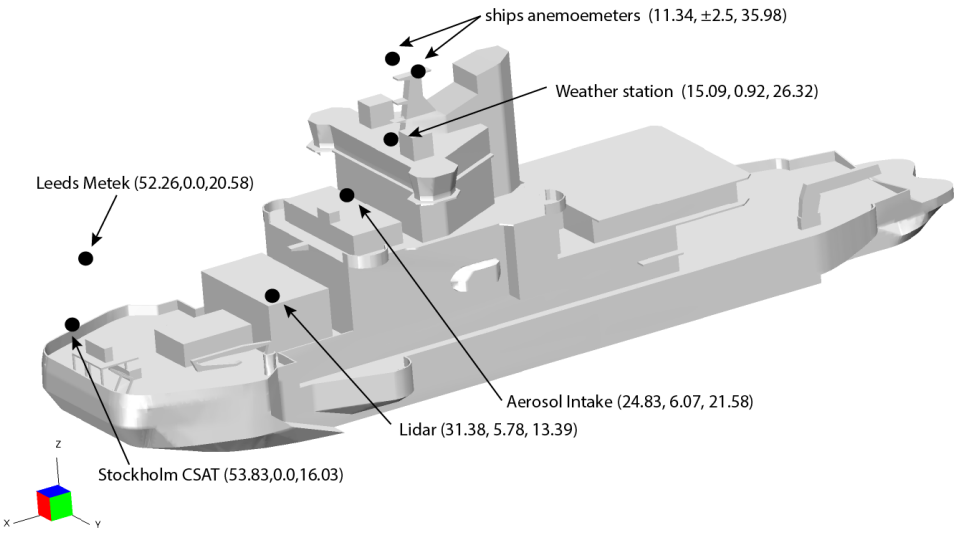

Figure 3.12: CAD model of Oden used by Moat et al. [26] to analyse the flow distortion of the wind sensors. The location of the anemometers is also shown as well.

The aerosol intake experienced a vertical streamline displacement of 6 m in a headwind, and 16 m in 90° wind. Indeed, real measurements by the lidar confirm that the ship's presence induces a significant upward velocity component to the flow. In summary, the flow simulations on Oden show that a ship can induce a significant amount of flow distortion on wind measurements.

3.3.2 Flow Distortion by the RV Knorr

The RV Knorr is a research ship that is well known for being the ship used to discover the wreck of the Titanic. In 1997, for the purpose of a wind measurement campaign in the Labrador Sea, a lattice tower with five wind sensors attached to it was placed on the bow of this ship. Another two wind sensors were attached to the bow mast, and one more was attached to the foremast, respectively [27]. A year later, Moat and Yelland [27] analysed the flow distortion in a headwind condition at the location of these sensors using a CFD simulation in. The CAD model of RV Knorr used in this simulation is presented in Figure 3.13, which also shows the location of the anemometers. Note that the lattice tower and bow mast were not included in this CAD model; thus, only the flow distortion due to the hull and superstructure could be simulated. Figure 3.13

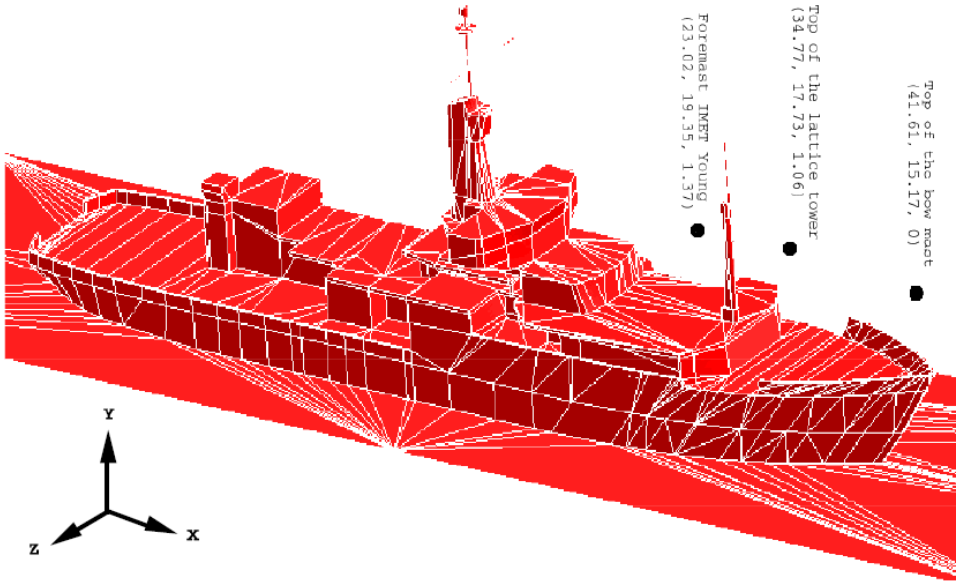

Figure 3.13: CAD model of RV Knorr used by Moat and Yelland [27] to analyse the flow distortion at the six anemometers. The location of the anemometers is also shown as well.

Just like Moat et al. [26], the incoming wind was modelled using a logarithmic profile, with a 10-meter wind speed of 15 m/s. No value for the other variables was specified. The simulation was time-dependent and performed with the Vectis solver, like Oden. The turbulence model used is not specified in the report. For the five wind sensors attached to the lattice tower, it was found that the wind had decelerated by roughly 0.8%, and the streamlines had displaced 0.75 m in the vertical direction, w.r.t. to the origin of the streamline. Thus, the exact location of the instruments attached to the lattice tower had no significant effect on the predicted flow distortion. [27]

The two instruments at the bow mast experienced a 2.0% flow deceleration w.r.t. the freestream and a 0.5 m vertical displacement, while at the foremast, a flow acceleration of 1% and vertical displacement of 1.3 m was found. These predictions at the foremast are likely inaccurate because, on the real ship, the foremast would have been in the wake of the lattice tower, which would cause more flow distortion. [27]

The flow distortion experienced by the sensors on RV Knorr is not as severe as that experienced by the sensors on Oden. This is not surprising, considering that the RV Knorr sensors were located on masts and were thus far from the influence of the superstructure, and the masts themselves were not present in the simulation. [27]

Chapter 4

Method

All the simulations in this project were performed using the commercially available CFD software Ansys Fluent version 2022 R2. The simulations were limited to steady-state cases using RANS turbulence models. The turbulence model employed was determined by conducting a validation study on the previously discussed Simple Frigate Shape 2. From this study, the Spalart-Allmaras turbulence model was selected for the simulations on MS Bard. Simulations were performed at seven different wind speeds ranging from 5 m/s to 30 m/s, and five wind directions between 0° and 180°.

This chapter describes the procedure through which the validation and the MS Bard simulations were performed. The validation method and its results are covered in Section 4.1, and the simulation procedure for MS Bard is detailed in Section 4.2.

4.1 Validation on SFS2

The simulation method for MS Bard was determined by creating a CFD model that could reproduce the experimental results from the study by Yuan et al. [4] on the Simple Frigate Shape 2. The main goal was to find the turbulence model that could most accurately replicate the velocity profiles shown in Figure 3.5. To this end, the Spalart-Allmaras, k-ω SST and k-ε turbulence models were compared to each other. The comparison was limited to the headwind velocity profiles on Map 1c in Figure 3.4. This section starts with a description of the CAD model and the computational grid, followed by the CFD set-up. After that, the simulation results, including the grid dependence study, are presented, and the turbulence model is subsequently selected.

4.1.1 Validation CAD Model

Figure 4.1 shows a drawing of the SFS2, that includes the dimensions in metres and the terminology relevant to this section. The ship's longitudinal, lateral and vertical axes are aligned with the x, y and z axes, respectively. The full-scale and model-scale dimensions are tabulated in Table 4.1.

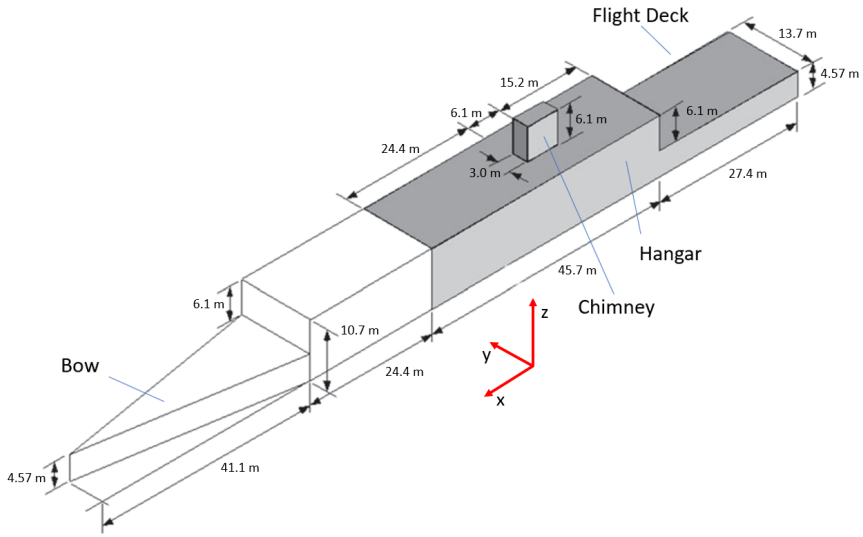

Figure 4.1: Modified version of the SFS2 drawing in Figure 3.1 that includes important terminology and the coordinate directions. From: Yuan et al. [4].

Table 4.1: Main dimensions of the SFS2 at full-scale and a 1:100 scale model. From: Yuan et al. [4].

Dimension	Full Scale Dimension (m)	Model Scale (m)
Overall length, L_{SFS2}	139.0	1.4
Beam, b_{SFS2}	13.7	0.1
Hangar height (w.r.t sea level)	10.7	0.1

A CAD model of the full-scale SFS2 was created with Solidworks version 29 to perform the validation. The initial version of the CAD model had an identical shape to the drawing shown in Figure 4.1, and is shown in Figure 4.2a. However, the mesh created from this CAD model resulted in a diverging mass residual during the simulations. It is believed that the calculated mass went up to infinity at the sharp edge. Thus, the decision was made to round the bow off to a radius of 1 m, resulting in the CAD model shown in Figure 4.2b. This modification to the bow was hypothesised to have minimal impact on the validation results because the test section described in Figure 3.4 is located far away at the stern of the ship.

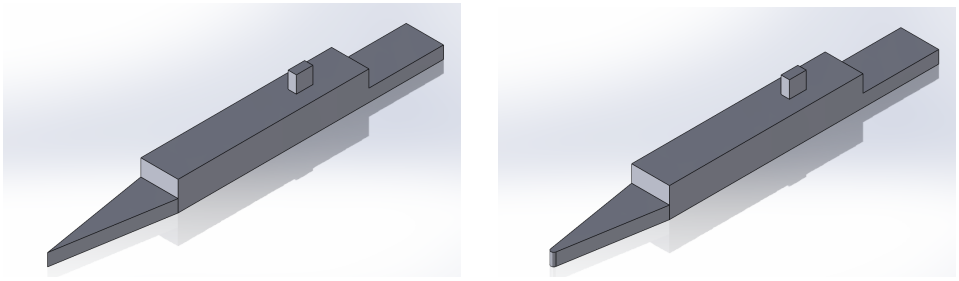

(a) Original SFS2 model.

(b) Modified SFS2 model with rounded bow. The bow radius is 1 m.

Figure 4.2: Two different versions of the SFS2 CAD model. Created with Solidworks version 29.

4.1.2 Validation Domain and Mesh

The domain used in the validation was created using the meshing software Pointwise, version 18.4 R3. It consisted of a cuboid shape that bounded the far-field, at the centre of which the SFS2 CAD model was located. The surface of the CAD model was integrated into the bottom boundary by cutting out the hull bottom and placing the waterline flush with the cuboid bottom. The remaining part of the cuboid bottom acted as the water surface. A schematic drawing of the domain is shown in Figure 4.3. To minimise the influence of the boundaries on the flow field near the ship, the horizontal domain dimensions were 30 times the ship's length, and the domain height was 15 times this length. The origin of the domain is located at the stern, on the ship centreline, at the bottom of the domain.

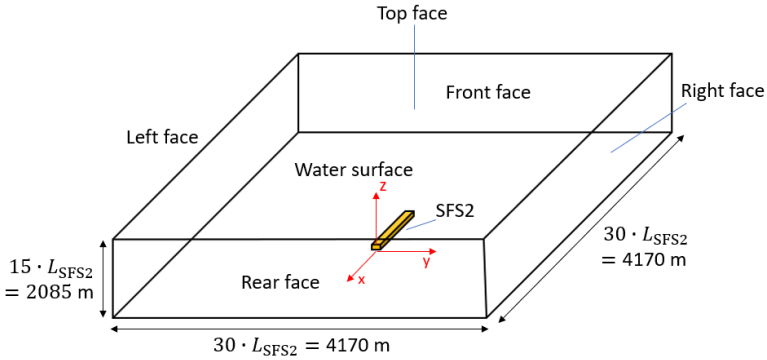

Figure 4.3: Schematic drawing of the simulation domain used in the validation. Includes the coordinate system.

The total number of cells within the validation grid was 9.9 million. The sides and top surfaces of the grid were made of an isotropic mesh, with a 50 m cell size on average. Likewise, the mesh on the ship's surface was isotropic, with a constant average cell size of 0.35 m. Mesh inflation was applied to the ship's surface, with a starting cell height of 0.03 m. This procedure covers the ship's surface with prismatic cells that gradually grow larger with distance from the surface. This mesh inflation was also imposed on the water surface mesh around the ship. The rest of this mesh was isotropic, with a cell size varying from 0.3 m at the last inflation layer to 50 m at the domain boundary.

The entire CAD model was enclosed by a source box. In Pointwise, a source box defines a volume within which a certain cell size can be specified. A smaller source box that enclosed the superstructure and the flight deck was placed within the larger one. The source boxes are drawn in Figure 4.4. The large and small source boxes are called Source 1 and Source 2, respectively, and have respective internal cell sizes of 0.84 m and 0.39 m.

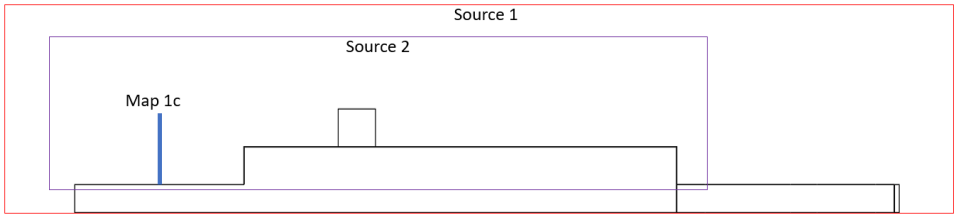

Figure 4.4: Schematic drawing of the source boxes applied to the SFS2 grid.

4.1.3 Boundary Conditions

The boundary conditions used in the validation simulation are summarised in Table 4.2. The top, left, and right faces of the grid had a symmetry boundary condition to represent the free-stream. The front face had a velocity inlet boundary condition, and the rear face had a pressure outlet condition with 0 Pa gauge pressure. The ship's surface had a no-slip

wall condition applied to it. Lastly, the water surface had a wall condition with zero shear stress, which is the same as the SFS2 simulations by Yuan et al. [4].

Table 4.2: Boundary conditions for the validation simulation.

Boundary	Condition	Parameter setting
Top face	Symmetry	-
Left face	Symmetry	-
Right face	Symmetry	-
Front face	Velocity inlet	Inlet speed: 0.58 m/s
Rear face	Pressure outlet	Gauge pressure: 0 Pa
Water surface	Wall	Shear stress: 0 Pa
Ship surface	No-slip wall	-

The inlet velocity was based on the Reynold's number used in the experiment by Yuan et al. [4]. They used a Reynold's number of $5.4e5$ for the headwind case, with a model scale velocity of 60 m/s and a characteristic length equal to the model ship beam. The dynamic viscosity and the density of the air were not specified. The validation simulation was performed with a full-scale CAD model of the SFS2. Thus, to maintain the Reynold's number of the experiment, a new inlet velocity had to be determined using Equation 2.3. The full-scale beam was used as characteristic length, and the standard values from Ansys Fluent were chosen for the kinematic viscosity and density. These values are $1.79\text{e-}5\,\mathrm{kg}/(\mathrm{m}\cdot\mathrm{s})$ [28] and $1.23\,\mathrm{kg}/\mathrm{m}^3$ [29] , which apply to an air temperature of 15°C in standard conditions. The new inlet velocity U was determined to be 0.58 m/s. The exact values used in the calculation are tabulated in Table 4.3.

The selected values for U, ρ, μ and l, combined with the first cell height on the ship's surface of 0.03 m, resulted in a $y+$ value of roughly 53. If the ship's overall length is used as the characteristic length, $y+$ becomes about 45. The determination of a characteristic length is subjective to some extent. In either case, the $y+$ value is well above the upper limit of the logarithmic layer, which implies that the validation simulation would not be able to model the inner parts of a turbulent boundary layer. This high $y+$ value was primarily chosen due to constraints in computation power, limiting the total number of cells within each simulation to around 10 million. A slight decrease in first cell height led to a significant increase in the total number of cells.

Table 4.3: Values used to calculate the inlet velocity for the validation simulation.

Parameter	Validation Sim.	Unit
Re	5.4e5	-
l	13.7	m
ρ	1.23	kg/m^3
μ	1.79e-5	$\mathrm{kg}/(\mathrm{m}\cdot\mathrm{s})$
ν	1.46e-5	m^2/s
U	0.58	m/s

4.1.4 Grid Dependence Study

When performing a numerical simulation, the results of the simulation should be checked for grid dependency. Grid dependency is when the result of a numerical simulation changes significantly when the grid changes. Thus, the grid introduces discrepancies into the simulation, decreasing the accuracy of the results. Grid dependence can be tested by repeating the simulation with a coarser and a finer mesh. If the simulation is grid-independent, the results should converge to a single value with increasing mesh resolution [10]. This is called grid convergence.

The grid dependence study was performed using the Spalart-Allmaras turbulence model. The coarse mesh was created by multiplying all the average cell sizes by $\sqrt{2}$, resulting in a coarse grid of 6.1 million cells. The fine mesh was created by dividing all the average cell sizes by $\sqrt{1.5}$ and had 15.7 million cells. The value for the x velocity component u, predicted at Map 1c, on the ship centreline at the height of the hangar roof, was used to evaluate the grid dependence. The value for u is plotted against the three mesh resolutions in Figure 4.5.

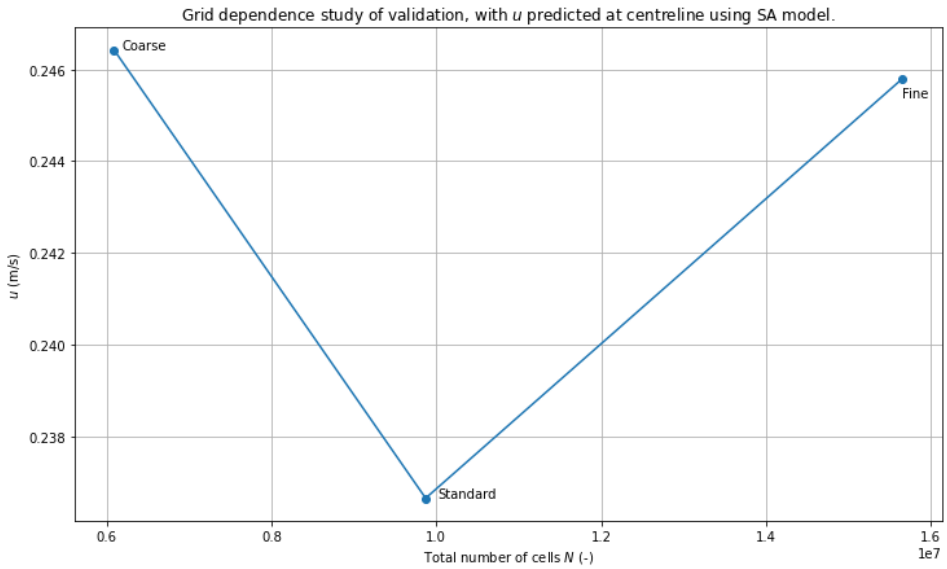

Figure 4.5: Predicted u velocity value at Map 1c, on the centreline at the height of the hangar roof, plotted against the total number of cells N.

Figure 4.5 shows that the value of u does not converge as the total number of cells increases. This implies that the simulation results experience some grid dependence. However, the difference between the u value predicted by the standard mesh and the other meshes is small. The u value from the coarse mesh is 4.1% larger than that of the standard mesh, and the u value of the fine mesh is 3.9% larger.

The similarity between the three mesh results is further illustrated by Figure 4.6, which

presents the lateral u velocity profiles on Map 1c at the height of the hangar roof. The y coordinate has been normalised by the ship beam b_{SFS2}. The black bars mark the outermost contours of the ship.

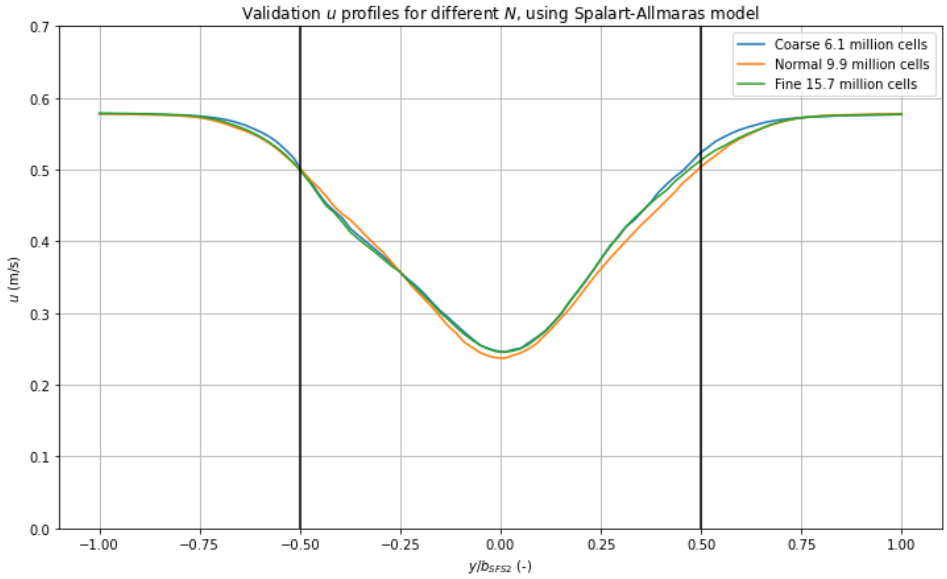

Figure 4.6: Comparison between the velocity profiles of the u component on Map 1c at hangar height predicted with the coarse, standard and fine mesh.

All three velocity profiles are quite similar, particularly those of the coarse and fine mesh. The largest deviation between the coarse and the standard velocity profiles is roughly 4.9% w.r.t. the standard profile and found at $y/b_{SFS2} \approx 0.40$. The greatest difference between the standard and the fine velocity profiles is found at $y/b_{SFS2} \approx 0.33$, and is about 4.7% w.r.t. the standard profile.

The grid dependence study showed evidence of grid dependence in the validation simulations when the Spalart-Allmaras turbulence model was used. However, it also showed that the effect of the grid dependence on the predicted u velocity profile at Map 1c is minor. Therefore, it is assumed that the effect of grid dependence on the other validation results will also be minor.

4.1.5 Validation Results

The streamline plots for all three turbulence models are presented in Figure 4.7. The yellow dot shows the location of Map 1c at the height of the hangar roof. All three streamline plots look similar, implying that all the turbulence models predict a similar flow field. Furthermore, the yellow dot is located in a flow region without recirculation in all three figures. This suggests that the predicted flow field in this area is accurate to reality, as RANS models are suitable for turbulent flows without turbulent structures [10].

Moreover, the streamlines at the stern of the ship appear to be mostly isolated from the streamlines at the bow. This lends credence to the assumption that changing the sharply pointed bow into a rounded bow does not significantly affect the flow field at the stern.

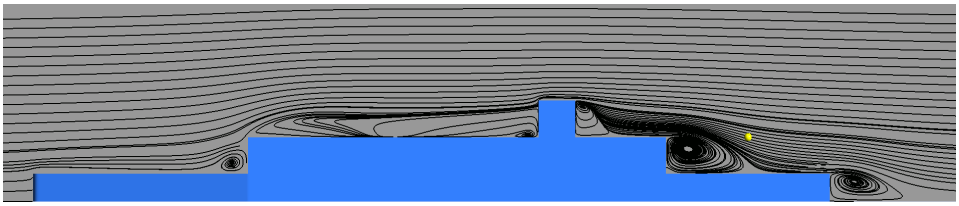

(a) Spalart-Allmaras

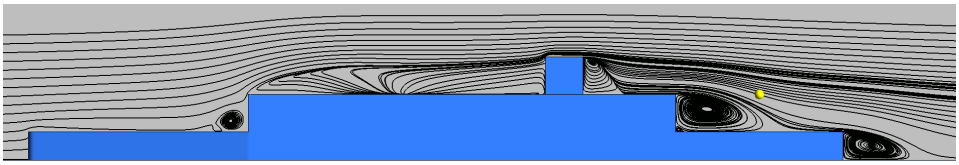

(b) k-ω SST

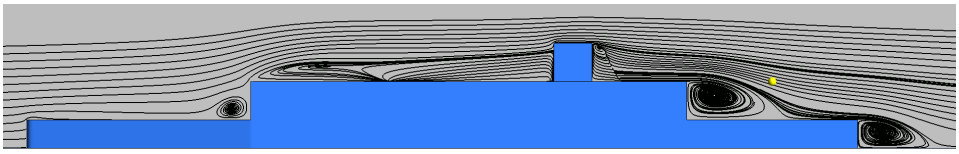

(c) k-ε

Figure 4.7: Simulated streamline plots for the validation simulation with each turbulence model. The yellow dot marks the location of Map 1c at the height of the hangar roof.

Figure 4.9 and Figure 4.11 present the simulated u (longitudinal) and v (lateral) velocity profiles at Map 1c, for the different turbulence models. The velocity components were normalised with the incoming flow speed U. The variable on the horizontal axis is the y-coordinate, normalised with the beam b_{SFS2}. The vertical black lines mark the outermost contour of the ship. Both plots also include the experimental data from Yuan et al. [4], shown previously in Figure 3.5.

The u-velocity profile in Figure 4.9 shows that none of the turbulence models closely

matches the experimental data. For all three turbulence models, the difference with the experimental case is more significant within the ship's beam than outside of it. The largest deviations are found around the centreline, within the convex part of the simulated curves. At $y/b_{SFS2} = -0.03$, which is the location of data-point A, the SA, k-ω SST and k-ε models respectively predict u/U values that are 39.8%, 39.3% and 45.1% lower than the experimental data.

Furthermore, the SA and k-ε models show the symmetry that is expected from the headwind case, while the k-ω SST model predicts more significant asymmetry. The experimental data also shows some asymmetry, but this was merely noted by Yuan et al. [4] and not analysed further. Moreover, their CFD results in Figure 3.5 did not predict asymmetry either. The difference between the u/U values in the experimental curve at $y/b_{SFS2} = -0.43$ and $y/b_{SFS2} = 0.43$ is roughly 13.2%. The reason for the asymmetry in the experimental data is not known.

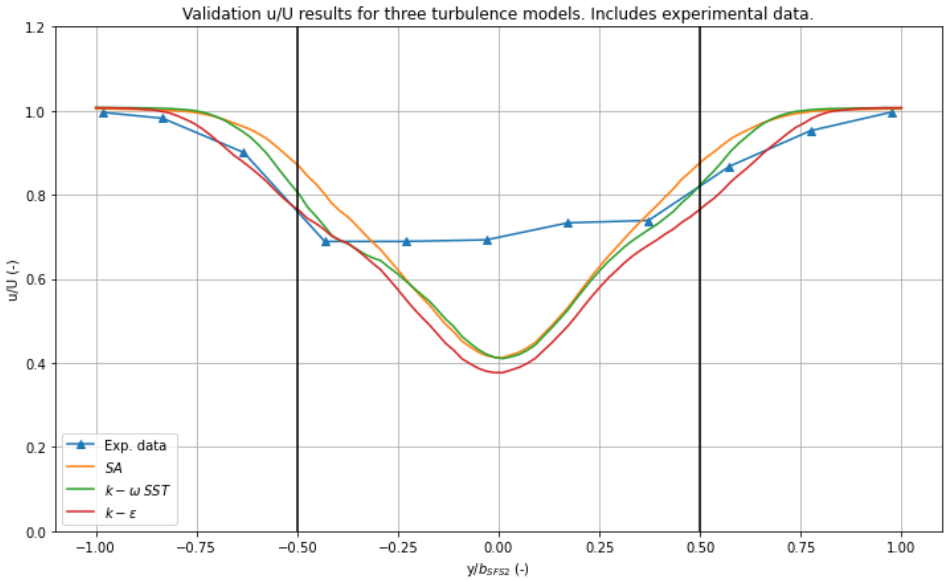

Figure 4.9: u velocity results from the validation simulations, normalised with the incoming flow speed U. Includes the turbulence models SA, k-ω SST and k-ε, and experimental data from Yuan et al. [4].

The convex part of the simulated curves in Figure 4.9, referred to as "valleys" for simplicity, are not present in either the experimental data or the CFD results (Figure 3.5) from Yuan et al. [4]. Figure 4.6 in the Grid Dependence Study also shows that the valleys occur for both the coarse and fine meshes as well. Thus, the presence of the valleys is probably not related to grid resolution. However, a similar valley was observed by Su and Xu [22], who also validated their CFD code using the SFS2 model in a headwind condition, and employed the k-ω turbulence model. Figure 4.10 compares their results to the predictions

from the SA model and the experimental data. The results by Su and Xu [22] are referred to as "Nanjing". Note that the Nanjing velocity profile is also asymmetric, suggesting that this results from an inherent property of the k-ω turbulence model.

The valley predicted by the SA simulation is 23.2% deeper than the one predicted by Su and Xu [22]. Thus, the latter is in closer agreement with the experimental data. The reason for this closer agreement is unknown, as Su and Xu [22] provided little detail on their computational set-up or the mesh. Nonetheless, the fact that an unsteady k-ω simulation also produces such a valley suggests that it is not the result of the steady-state assumption, and the valleys might be a characteristic of RANS models.

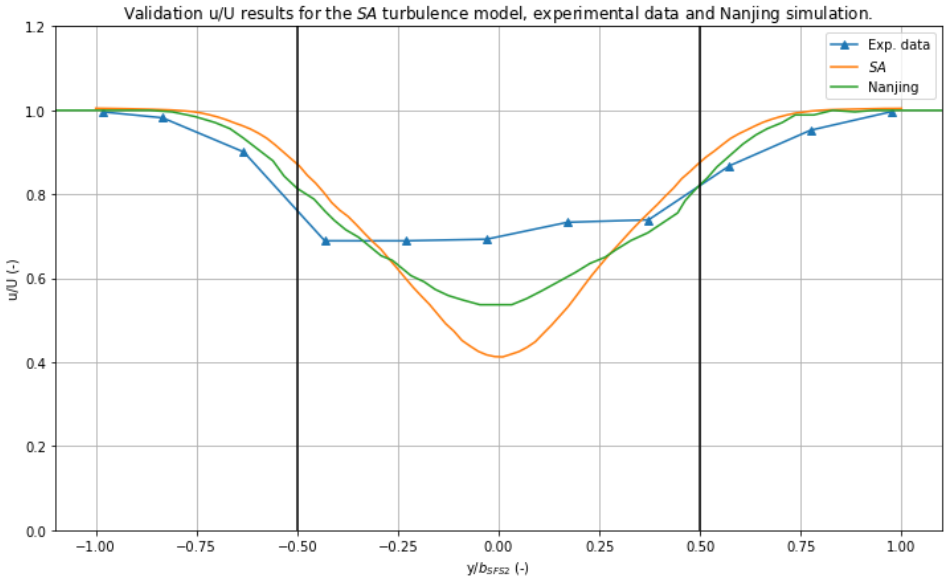

Figure 4.10: Comparison of the u velocity results from the steady SA model, the unsteady k-ω from Su and Xu [22], and experimental data from Yuan et al. [4].

The normalised v-velocity predicted by the turbulence models in Figure 4.11 is in better agreement with the experimental data than the u-velocity predictions. The v-velocity predictions are more accurate within the ship's beam than outside of it. Within the beam, all three turbulence models predicted a slightly less steep velocity gradient than the experiment. Outside the beam, the k-ε model is in closest agreement with the experimental data, while the other two turbulence models tended to over-predict the magnitude of the v component. The maximum differences between the predictions and the data are 19% and 24% for the SA and k-ω SST models, respectively, and occur at the positive extreme values.

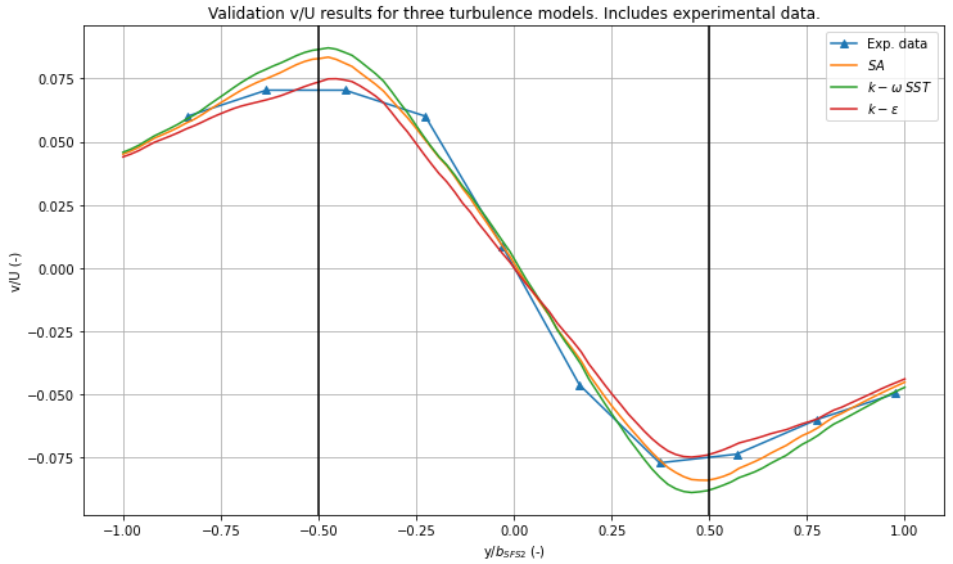

Figure 4.11: v velocity results from the validation simulations, normalised with the incoming flow speed U. Includes the turbulence models SA, k-ω SST and k-ε, and experimental data from Yuan et al. [4].

Despite the presence of the valleys in the normalised u velocity profiles, the agreement between the current simulation method and the experimental data is assumed to be good enough to use this method for the MS Bard simulations. While no turbulence model outperformed the others in accuracy, a single model had to be selected regardless due to time constraints. Even though each model has its speciality, the similarity in the validation results suggests that these specialities make little difference. Thus, the model was primarily selected based on the few visible differences in the validation results and practical grounds.

Both the Spalart-Allmaras and k-ε models showed the symmetry that was expected in the u/U plot. Being a one-equation model, the SA model is also the simplest and thus computes iterations faster than the other two [14]. The k-ε turbulence model does show better agreement for the v/U results, but its use of wall functions makes it slower. While the k-ω SST model is not slowed down by wall functions, its nature as a two-equation model still makes it slower than the SA model, and its asymmetric prediction is concerning. Thus, the Spalart-Allmaras turbulence model was selected for the MS Bard simulations. However, due to the uncertainty in this selection, a couple of MS Bard simulations would be repeated with the other two turbulence models.

4.2 MS Bard Simulation Method

This section discusses the simulation procedure for MS Bard. The simulations were performed at horizontal wind angles θ ranging from 0° (headwind) to 180° (tailwind), at 45° intervals. These angles are defined in Figure 4.12. The incoming wind was modelled using a power law wind profile, with the wind speed at the sensor height varying from 5 m/s to 30 m/s at 5 m/s intervals. The computational domain was similar to the validation domain, employing the same boundary conditions. All simulations were performed using the Spalart-Allmaras turbulence model, but the 15 m/s headwind and 90° cases were repeated with the k-ε and k-ω SST model.

The section starts with a description of MS Bard and the wind sensor. This is followed by an explanation of the CAD model and the computational set-up, including the wind profile. Lastly, a description of the computational domain and the grid is provided.

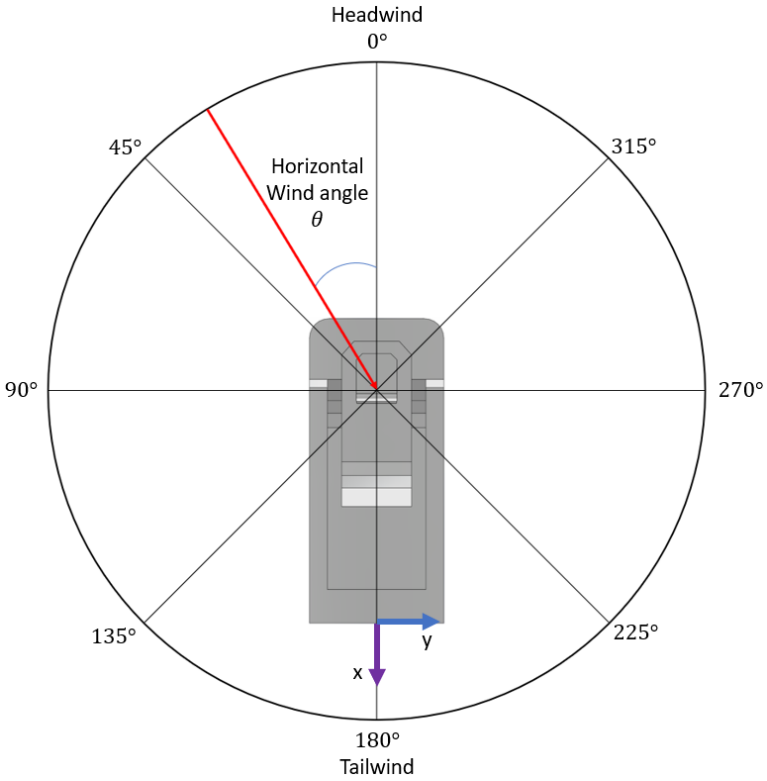

Figure 4.12: Diagram showing the horizontal wind angle definitions.

4.2.1 Ship Description

The ship on which the wind sensor is placed is MS Bard, shown in Figure 1.2, which is a hybrid-electric catamaran owned by Hurtigruten Svalbard AS [3]. This boat sails around the Svalbard archipelago, ferrying tourists from Longyearbyen to the coal mining town of Barentsburg and the abandoned town of Pyramiden. The main dimensions of MS Bard are presented in Figure 4.13, which includes the location of the wind sensor. The ship has an overall length of 24.80 m, a maximum beam of 11.00 m, and an above-water height of 9.55 m [30]. The wind sensor is located at the height of 12.20 ± 0.10 m, at 0.27 ± 0.05 m towards the starboard side, and 18.70 ± 0.10 m from the ship's stern. The error margin results from the difficulty in measuring these distances.

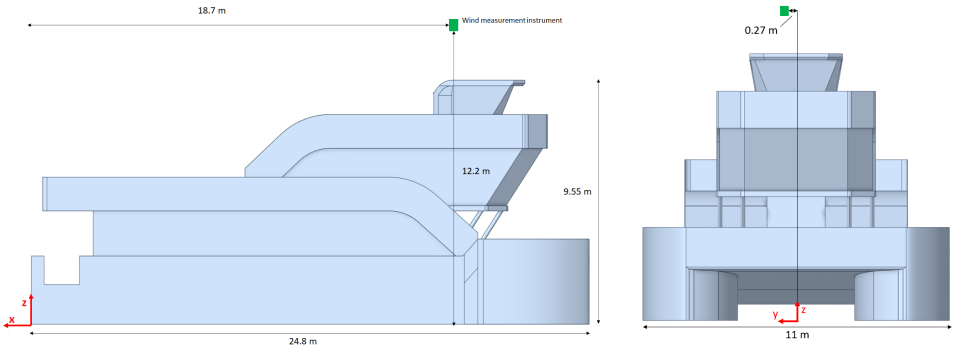

(a) Side view. **(b)** Front view.

Figure 4.13: Drawing of MS Bard, including the main dimensions, the sensor location and the coordinate system. Created with Solidworks version 29. The dimensions were retrieved from Marine Traffic [30].

Table 4.4: Main dimensions of MS Bard and wind sensor location. The dimensions are from [30].

MS Bard Dimensions	
Dimension	**Value (m)**
Overall length, L_{bard}	24.80
Beam, b_{bard}	11.00
Height w.r.t. water level	9.55

Wind sensor location	
Coordinate	**Value (m)**
x	-18.70
y	0.27
z	12.20

4.2.2 Wind Sensor Description

The wind sensor on MS Bard is the Gill MaxiMet GMX 500, manufactured by Gill Instruments Ltd. [31]. A picture and technical drawing of the instrument are presented in Figure 4.14. The instrument is attached to the radar mast on top of the bridge of MS Bard. The Gill MaxiMet GMX 500 can measure wind speed and direction, temperature, humidity and pressure [31]. Only the wind direction and speed are relevant in this project and will thus be discussed further in this section.

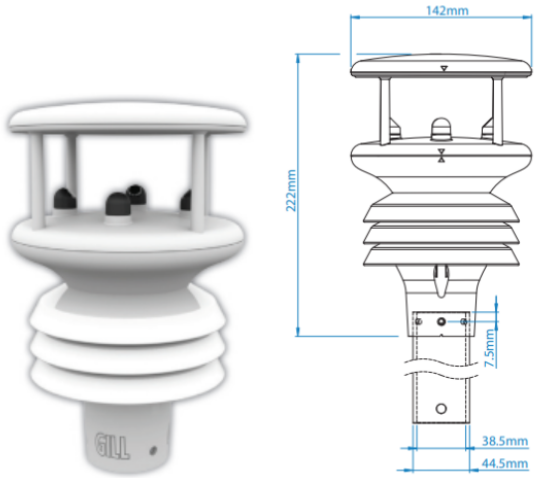

Figure 4.14: Picture and technical drawing of the MaxiMet GMX500. From: Gill MaxiMet Ltd. [31].

The wind sensor can measure wind speed in a range of [0.01, 60.0] m/s with a 0.01 m/s resolution, and wind direction in a range of [0, 359] degrees with a 1° resolution [31]. These measurements provide the apparent wind, which is the wind measured by an observer moving with the ship. The ship's speed and directional data acquired by GPS are then used to correct the apparent wind to retrieve the true wind speed and direction [31]. This is the wind as measured by a stationary observer. It is important to note that true wind corrects only for the ship's movement and not for its flow distortion, which is the goal of this project.

The device used to measure wind speed and direction is an ultrasonic anemometer. It consists of an ultrasonic sound emitter and a receiver, which are at a known distance apart. The time it takes for ultrasonic waves to travel between the emitter and receiver is affected by the wind component in the travel direction of the waves [32]. Thus, the wind causes the ultrasonic wave speed to deviate from the speed of sound in still air [32]. The difference between these two speeds is used to calculate the wind speed [32]. Furthermore, combining three pairs of emitters and receivers makes it possible to determine the complete wind vector [32].

4.2.3 MS Bard CAD Model

A simplified CAD model of MS Bard was created with the CAD software Solidworks, version 29. Everything but the main outlines of the ship was removed. The stairs were replaced by ramps, and all exterior floors were raised to be flush with the railings visible in Figure 1.2. The windows were also made flush with their frames. Furthermore, the sides of the two hulls were changed to make them stick out from the water perpendicularly. The simplified CAD model is presented in Figure 4.15.

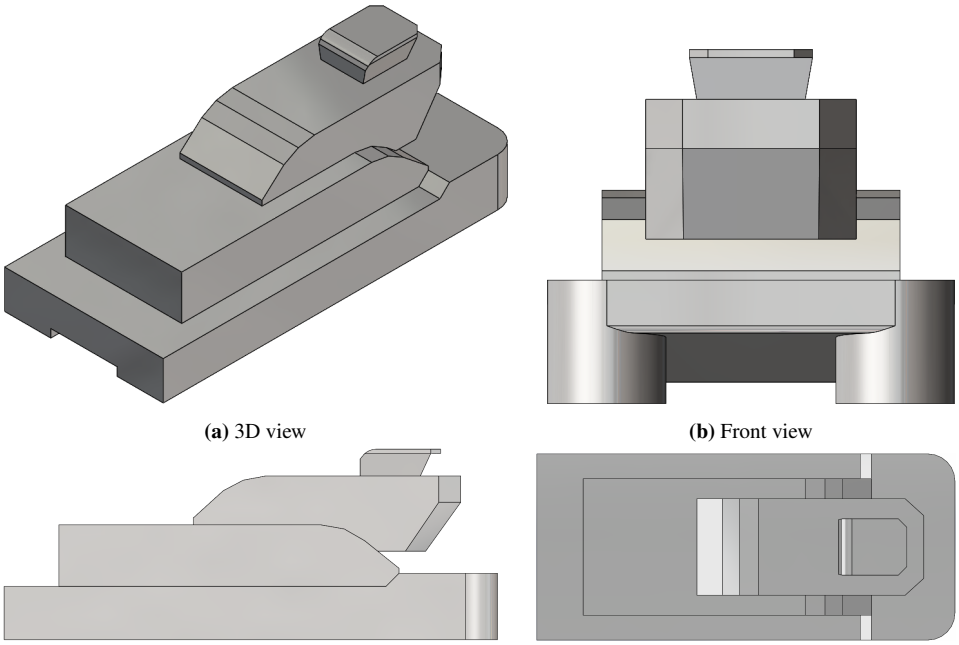

(a) 3D view

(b) Front view

(c) Starboard side view

(d) Top view

Figure 4.15: CAD model of MS Bard in four different views: (a) 3D view, (b) front view, (c) side view, (d) top view. Created with Solidworks version 29.

The simplified CAD model deviates significantly from the actual ship, but the level of simplification is still comparable to that of the megayacht CAD model employed by Trivyza and Boulougouris [9] (Figure 3.9). However, unlike the MS Bard CAD model, the megayacht CAD model does include a complicated hull shape. This is understandable as the purpose of that paper was to investigate the overall aerodynamics of a megayacht, and the hull makes up a large part of its above-water structure. On the other hand, the hulls of MS Bard make up a much smaller part of the overall above-water structure, and the lower deck blocks their influence on the flow field at the measurement device. Thus, simplifying the two hulls is not expected to affect the flow field near the wind sensor significantly.

4.2.4 Computational Set-Up

The simulations on MS Bard were performed using almost the same set-up as the validation simulations. The flow was assumed incompressible and modelled in steady-state. The RANS turbulence model employed for all simulations was Spalart-Allmaras. Unlike the validation, the MS Bard simulations were performed with air at 0 °C. This is roughly the average temperature in Longyearbyen between May and October when MS Bard operates [33]. The associated dynamic viscosity and density are $1.72\text{e-}5\,\mathrm{kg}/(\mathrm{m}\cdot\mathrm{s})$ [28] and $1.29\,\mathrm{kg}/\mathrm{m}^3$ [29], respectively, in standard atmospheric conditions.

Wind Profiles

In the validation, the incoming wind was modelled with a constant velocity profile that did not vary with height. For the MS bard simulations, a varying wind profile was applied. The overall height of MS Bard is within the height of the surface layer, which can be several hundreds of metres high [16]. The logarithmic wind profile is the most accurate in this region [16], but requires the roughness length z_0 as input data, which was difficult to acquire. Therefore, the incoming wind profile was modelled using a power law, which was also used by Forrest and Owen [17] and Wang et al. [18] in their simulations. The expression for a power law profile is repeated here for the reader's convenience:

$$U = U_{ref}(\frac{z}{z_{ref}})^{\alpha}, \tag{4.1}$$

The incoming wind profile was assumed to be constant in the lateral direction. z_{ref} was equal to the z-coordinate of the wind sensor (12.2 m), and U_{ref} was the incoming flow speed. Thus, without any flow distortion by the ship, the flow velocity at the sensor location would equal U_{ref}. As a result, any deviation from the reference velocity would have to result from flow distortion.

The value for alpha had to be found in the literature. According to Wang et al. [18], the value of α is typically between 0.11 and 0.14 for velocity profiles over the ocean. This range initially came from the 1997 Norwegian Maritime Directory, but this source is no longer available. Wang et al. [18] ended up using an α value of 0.125 for their study on cruise ships. This value is very close to the 0.13 employed by Forrest and Owen [17] for their flow simulations on the SFS2. Another commonly used value is 0.143, or 1/7, which approximates the wind profile of an atmospheric boundary layer over land very well [34]. It is not clear how accurate this value is for wind over water.

Under the assumption that a slight change in the value of α would not significantly affect the simulation results and the correction method, and to stay within the 0.11 to 0.14 range given by Wang et al. [18], a value of 0.14 was selected for α. To ensure the accuracy of the previous assumption, the 15 m/s headwind simulation would be repeated with an α value of 0.13 and 0.15, and the results will be compared.

Flow Cases

Simulations were performed for a limited number of wind speeds and directions: 5 m/s, 10 m/s, 15 m/s, 25 m/s and 30 m/s, and 0°, 45°, 90°, 135°and 180°, respectively. The CAD model of MS Bard is symmetric; thus, the results for the angles 45°, 90° and 135° can be mirrored to the other side.

Unlike in the validation, not all MS Bard simulation cases had the same Reynold's number. This is because the Reynold's number depends on wind speed and wind angle. The wind angle is important because it changes the characteristic length l, which is one of the variables in Equation 2.3. For the headwind and tailwind cases, l was the ship's length, and for the 90° case, l was equal to the beam. For the 45° and 135° wind angles, the characteristic length was the diagonal dimension of the ship, which is 27.1 m. The Reynold's number for each wind angle and wind speed combination is given in Table 4.5.

Table 4.5: Reynold's number for each wind angle and wind speed combination in the MS Bard simulations.

	Reynold's Number (10^6)				
U **(m/s)**	**0°**	**45°**	**90°**	**135°**	**180°**
5	9.3	10.2	4.1	10.2	9.3
10	18.7	20.4	82.9	20.4	18.7
15	28.0	30.7	12.4	30.7	28.0
20	37.4	40.9	16.6	40.9	37.4
25	46.7	51.1	20.7	51.1	46.7
30	56.0	61.3	24.9	61.3	56.0

4.2.5 MS Bard Domain and Mesh

Two different mesh domains were created for the simulations on MS Bard, called Domain A and Domain B, both created in Pointwise, version 18.4 R3. Both domains had cuboid shapes with identical sides. The top view of both domains is shown in Figure 4.16. The only difference between the two is that Domain B is rotated 45° about the z-axis. Domain B was used for the 45° and 135° simulations, while Domain A was employed for the remaining angles. Like the validation domain, the horizontal dimensions were each 30 times the length of MS Bard, and the height 15 times this length. Both domains were set up in the same way as the validation domain. The ship surface was integrated into the bottom boundary, and the remaining bottom area acted as the water surface.

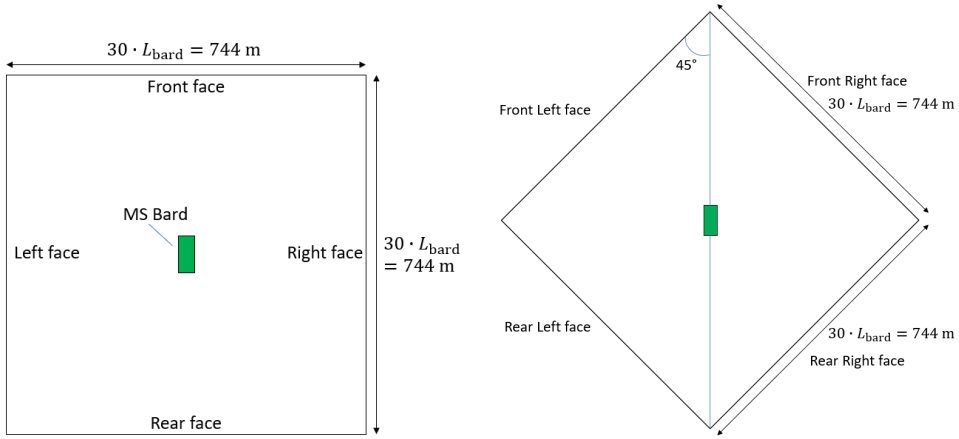

(a) Domain A **(b)** Domain B

Figure 4.16: Schematic drawing of Domain A and Domain B used for the MS Bard simulations. Domain B is the same as A, but rotated 45° about the z-axis.

To ensure that the conclusions from the validation results would be applicable to the MS Bard simulations, the ratio between the total number of cells in the grid N and the beam of each ship b had to be the same. The resulting number of cells required for the MS Bard simulations was around 8 million. Through the mesh generation process, N ended up being 7.95 million cells in Domain A and 7.97 million cells in Domain B. It would also have been possible to use the ratio between N and the ship length L, but this resulted in a required number of cells of only 1.8 million for MS Bard. This would not be enough to mesh the relatively complex CAD model accurately.

In both Domain A and B, an isotropic mesh with an average cell size of 50 m was applied to the domain boundaries. The ship's surface's mesh resolution increased with height, starting with 0.28 m at the hull. The surface resolution on the first storey was 0.21 m, and it was 0.14 m on the second story. Lastly, the grid size on the bridge surface was 0.11 m.

The $y+$ value in the validation simulations was either 45 or 53, depending on the reference length used to calculate it. The lower value should lead to a more accurate simulation; thus, the mesh design aimed to reach a $y+$ of 45 for all MS Bard simulations. However, since $y+$ is related to incoming flow velocity and the reference length, this would require a different mesh for every wind speed and wind angle (the latter is relevant because it changes the reference length). This was not feasible, and thus it was decided that for all velocities and horizontal wind angles, the $y+$ value should be smaller or equal to 45. This was achieved by applying mesh inflation on the ship's surface, with an initial cell height of 0.59 mm. The mesh inflation was also imposed on the water surface mesh around the ship. The rest of the water had an isotropic mesh.

Three source boxes were used to generate the mesh: Source 3, Source 4 and Source 5. Source 3 encompassed the entire ship and applied a cell size of 0.28 m. Source 4 specified a 0.21 m cell size, and enclosed the second storey and the bridge. Finally, Source 5 en-

compassed the bridge and the sensor location, and enforced a 0.11 m cell size. The source boxes are presented in Figure 4.17. They were identical in both Domain A and B.

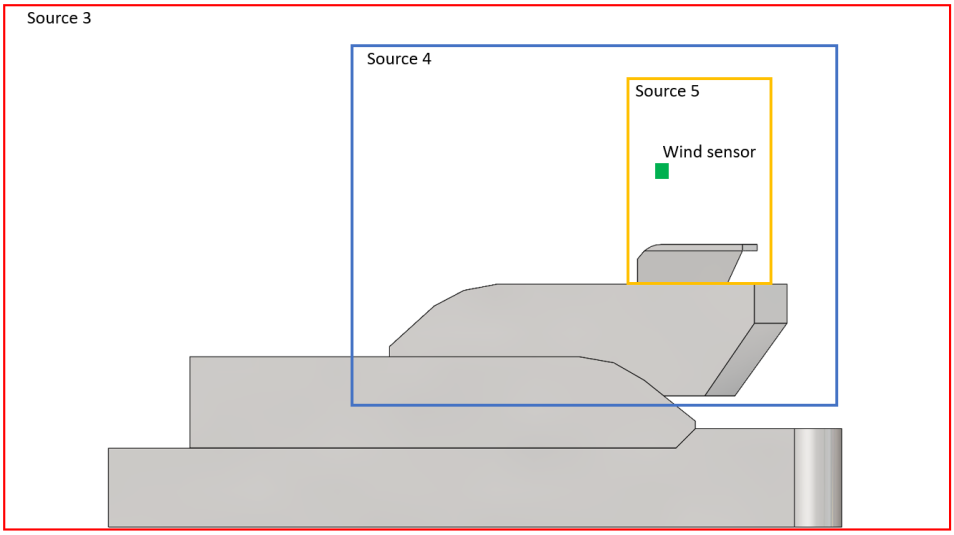

Figure 4.17: Schematic drawing of the source boxes applied to the MS Bard grid.

4.2.6 Boundary Conditions

The boundary conditions used in the MS Bard simulations were the same as the ones used in the validation case, but their locations changed to match the different wind angles. The boundary conditions for Domain A and Domain B are summarised in Table 4.6 and Table 4.7, respectively.

Table 4.6: Boundary conditions used in the MS Bard simulations for the headwind, tailwind and 90° flow cases. Applied to Domain A.

Domain A			
Boundary	**Headwind**	**Tailwind**	**90°**
Top face	Symmetry	Symmetry	Symmetry
Left face	Symmetry	Symmetry	Velocity inlet
Right face	Symmetry	Symmetry	Pressure outlet
Front face	Velocity inlet	Pressure outlet	Symmetry
Rear face	Pressure outlet	Velocity inlet	symmetry
Water surface	Zero shear wall	Zero shear wall	Zero shear wall
Ship surface	No-slip wall	No-slip wall	No-slip wall

Table 4.7: Boundary conditions used in the MS Bard simulations for the 45° and 135° flow cases. Applied to Domain B.

Domain B		
Boundary	**45°**	**135°**
Top face	Symmetry	Symmetry
Front Left face	Velocity inlet	Symmetry
Front Right face	Symmetry	Pressure outlet
Rear Left face	Symmetry	Velocity inlet
Rear Right face	Pressure outlet	Symmetry
Water surface	Zero shear wall	Zero shear wall
Ship surface	No-slip wall	No-slip wall

Chapter 5

Results

This chapter provides the results of the MS Bard simulations and discusses the implications and the accuracy of these results. The chapter starts with a grid dependence study of the 15 m/s headwind solution in Section 5.1. This is followed by Section 5.2, which discusses the predicted flow fields from the MS Bard simulations. Section 5.3 describes the velocity vector predicted at the sensor location for each flow case. Finally, the correction method is developed in Section 5.4.

5.1 Grid Dependence Study

In order to determine whether the MS Bard simulation results were subject to mesh dependence, the 15 m/s headwind simulation was repeated with both a coarser and a finer mesh. The cell sizes of the coarse mesh were a factor $\sqrt{2}$ bigger than the standard mesh, while the cell sizes of the fine mesh were a factor $\sqrt{2}$ smaller. The grid dependency study was only performed on Domain A because of time constraints. The turbulence model applied was Spalart-Allmaras. Figure 5.1 plots the wind magnitude at the sensor location against the total number of cells.

The figure shows that as the total number of cells increases, the predicted wind magnitude does not converge to a single value. This implies that the simulation results are grid-dependent. However, the velocity magnitudes from the coarse and fine meshes are only 0.3% larger than that of the standard mesh. Thus, the grid dependency is likely relatively small.

Furthermore, the grid dependence of the solution will likely have a minor effect on the accuracy of the correction method. This is because the biggest difference in simulated speed in Figure 5.1 is only 0.05 m/s. The sensor accuracy for wind speeds under 40 m/s is 3% [31]. If the incoming wind speed of 15 m/s is used as a reference, 3% will be 0.45 m/s. This is nine times greater than the 0.05 m/s difference in simulated speed. Thus, the effect of grid dependence is likely negligible compared to the sensor inaccuracy.

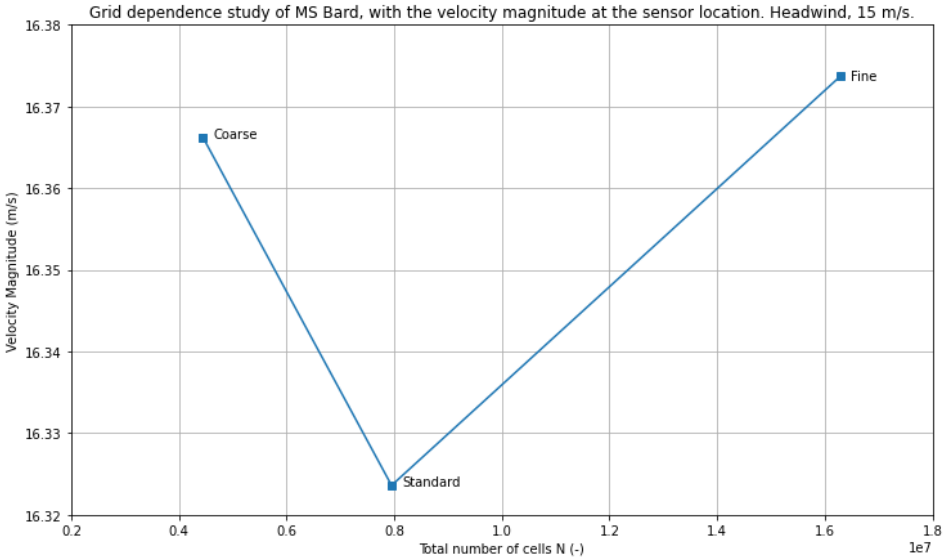

Figure 5.1: Predicted velocity magnitude at the sensor location plotted against the total number of cells N. For the 15 m/s headwind case.

5.2 MS Bard Simulated Flow Fields

The table below shows which simulations converged, diverged or were skipped. Seven simulations diverged at the higher speeds in the 90°, 135° and tailwind cases. These simulations were performed quite late in the project; thus, there was no time left to find the cause of the divergence. The 15 m/s, 20 m/s and 25 m/s simulations for the 45° case were not performed, because the results the 5 m/s, 10 m/s and 30 m/s cases showed strong signs that the flow field was independent of flow speed.

Table 5.1: Table showing which MS Bard flow cases converged, diverged or were skipped.

Incoming wind angle	5 m/s	10 m/s	15 m/s	20 m/s	25 m/s	30 m/s
Headwind	Con	Con	Con	Con	Con	Con
45°	Con	Con	Skip	Skip	Skip	Con
90°	Con	Con	Con	Div	Div	Div
135°	Con	Con	Con	Con	Con	Div
Tailwind	Con	Con	Con	Dive	Div	Div

5.2.1 Headwind Flow Field

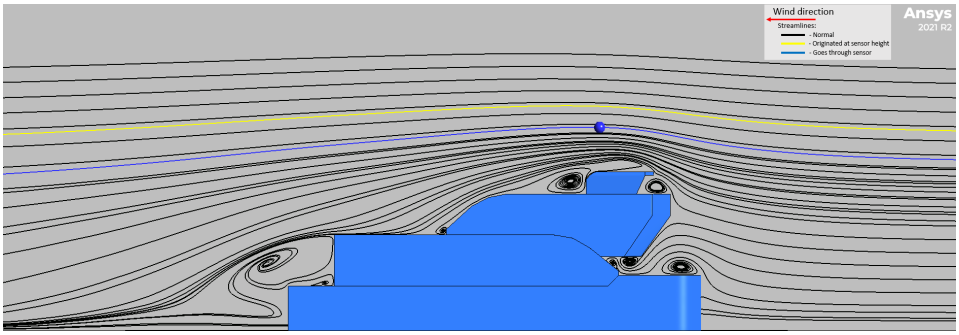

(a) Headwind 5 m/s.

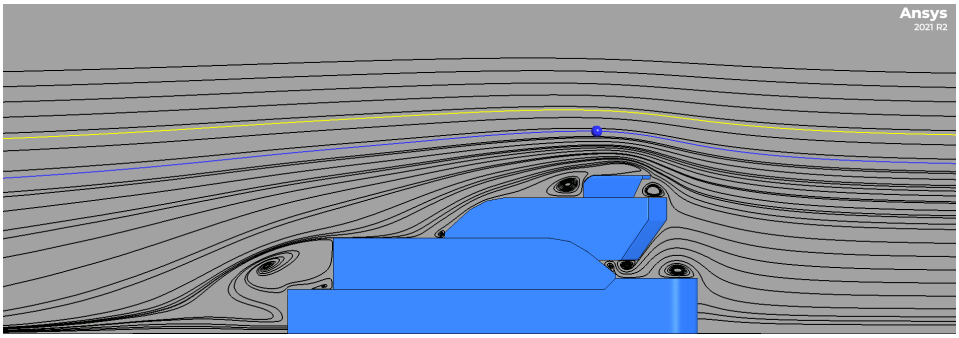

(b) Headwind 30 m/s.

Figure 5.2: Streamline plots for the headwind condition at wind speeds of 5 m/s and 30 m/s. The blue dot represents the wind sensor. The blue streamline goes through the wind sensor, and the yellow streamline is the one that originated at the sensor height of 12.20 m at the inlet.

Figure 5.2 shows the streamline plot of the wind flow over MS Bard in headwind condition, at incoming wind speeds of 5 m/s and 30 m/s. The blue dot shows the wind sensor's location, and the blue streamline is the streamline through this location. Similarly, the yellow streamline is the one that originated at the sensor height of 12.20 m at the inlet.

The first thing of note is that both plots show nearly identical streamlines, which suggests

that flow fields in the headwind flow cases are independent of velocity and by extension Reynold's number. Furthermore, note that the yellow streamline does not go through the sensor location, which is what would be expected if the ship would not distort the flow field. Instead, the blue streamline that goes through the sensor originated from a lower height of 10.50 m. The incoming wind speed at this location is around 4.89 m/s instead of 5.00 m/s, which is only a minimal difference.

Another noteworthy point is that the streamlines approaching the ship diverge, leading to a higher streamline density near the sensor location. Greater streamline density in incompressible flow usually implies an increase in flow speed. This is confirmed by Figure 5.3, which shows the velocity magnitude of the flow over the ship. Moreover, the streamlines near the sensor location appear to be quite simple and do not show any unsteady flow structures. RANS turbulence models are generally accurate for this type of flow field [10], which is evidence that the predicted velocity vector at the sensor location is representative of reality.

Furthermore, Figure 5.2 shows the occurrence of vortices in the wake of all the deck structures. The largest vortex is found behind the first-storey block, which is the highest block and ends at a 90-degree angle. The occurrence of flow separation and vortex formation in the wake of a ship superstructure is a common observation in ship aerodynamics [9, 17, 18], and the large vortex corresponds to the separation bubble behind the SFS2 superstructure observed by Forrest and Owen [17]. Furthermore, it seems that the flow follows the smooth contours of the ship and only separates when it reaches a relatively sharp angle in the geometry, which is generally the case with bluff bodies [24, 35]. This is in agreement with the conclusion by Hoxey et al. [25], that a wind flowing over a sharp angled roof separates, while wind flowing over a curved roof does not.

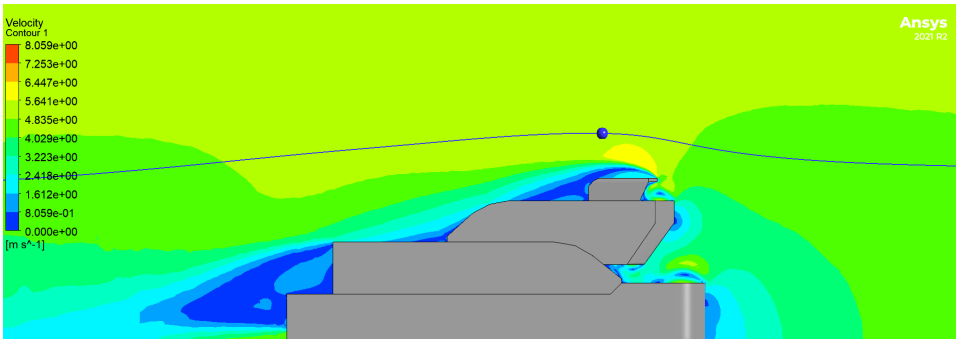

(a) Headwind 5 m/s.

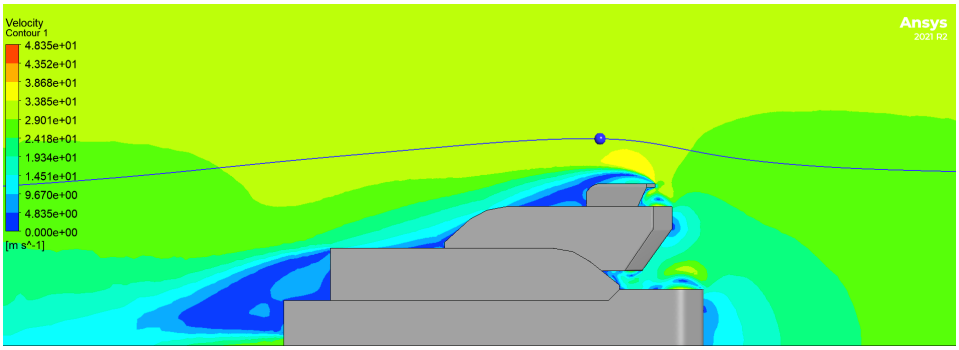

(b) Headwind 30 m/s.

Figure 5.3: Velocity magnitude contour plot for the 5 m/s and 30 m/s headwind cases.

5.2.2 90° Flow Field

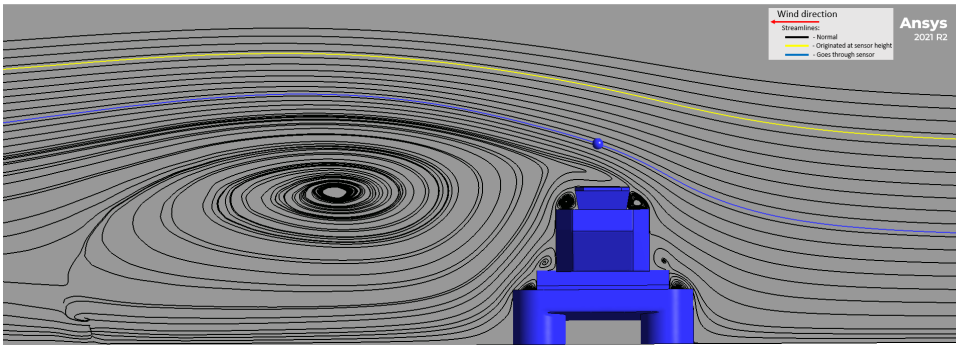

(a) 90°, 5 m/s.

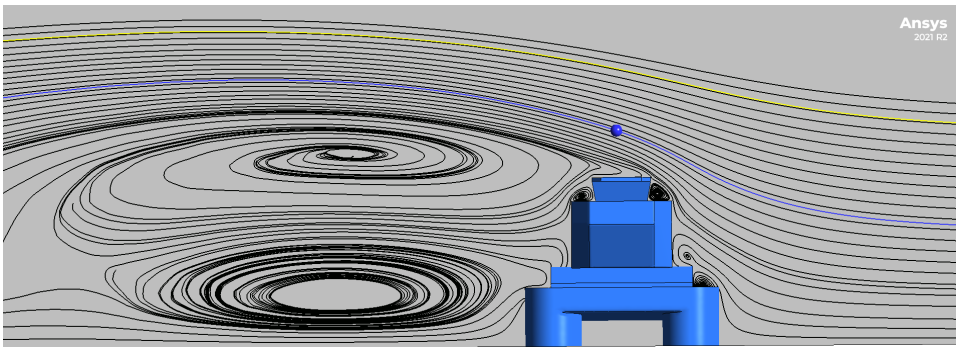

(b) 90°, 15 m/s.

Figure 5.4: Streamline plots for the 90° wind angle at wind speeds of 5 m/s and 15 m/s. The blue dot represents the wind sensor. The blue streamline goes through the wind sensor, and the yellow streamline is the one that originated at the sensor height of 12.20 m at the inlet.

Figure 5.4 shows that the Reynold's number independence observed in the headwind case is not present at the 90° wind angle. While the flow field on the windward side of the ship does not appear to change with speed, the leeward side does. At 5 m/s, a single large vortex was predicted on the leeward side, while at 15 m/s, it was replaced with two smaller vortices of similar size. The literature study did not reveal any other papers that observed this phenomenon; thus, the reason for it is not known.

The flow field near the wind sensor does not appear to change with wind speed, suggesting that the predicted flow at the sensor location is locally Reynold's number independent. Furthermore, like in the headwind case, the streamlines directly near the sensor do not show turbulent features, which suggests that the SA turbulence model can accurately predict the flow at the sensor. There does appear to be some flow separation just above the roof of the bridge, but the sensor is at least a metre above this area. Thus, the flow field there is unlikely to be affected by this local separation.

Note also that the streamline going through the sensor location is inclined upwards instead of horizontal. Thus, the w component of the velocity vector is not negligible at this location. Moreover, as in the headwind case, the blue streamline through the measurement location does not originate at the height of 12.20 m, but instead at 6.53 m. In the 5.00 m/s case, the flow speed at this height is around 4.58 m/s, which is a larger difference than in the headwind condition.

5.2.3 Tailwind Flow Field

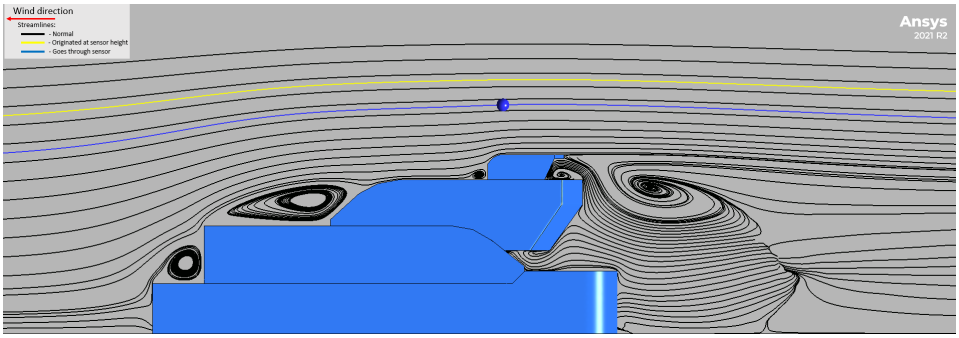

(a) Tailwind 5 m/s.

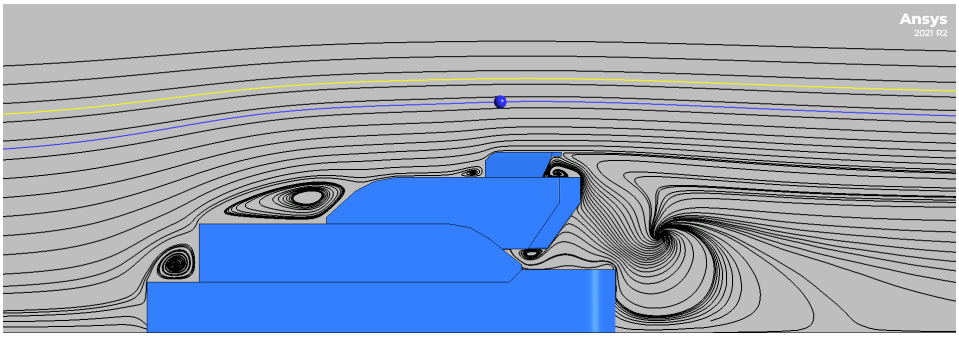

(b) Tailwind 15 m/s.

Figure 5.5: Streamline plots for the tailwind condition at wind speeds of 5 m/s and 15 m/s. The blue dot represents the wind sensor. The blue streamline goes through the wind sensor, and the yellow streamline is the one that originated at the sensor height of 12.20 m at the inlet.

The streamline plots for the 5 m/s and 15 m/s tailwind cases are presented in Figure 5.5. In general, both plots show similar flow fields. The streamlines are nearly identical at the stern side of the bridge and around the wind sensor. However, there are a couple of differences. The large vortex above the bow is located higher up in the 5 m/s case than in the 15 m/s case. Beyond the differences between the two incoming velocity magnitudes, the tailwind results show a flow field similar to what would be expected when reversing the headwind case.

As with the headwind and 90° cases, the blue streamline through the sensor location does not originate at the sensor height, but at a height of 10.80 m. This corresponds to an incoming flow speed of about 4.91 m/s in the 5.00 m/s case, which is similar to the headwind case. Furthermore, the flow field around the sensor does not show any turbulent features, suggesting the flow predictions in this area are realistic.

5.2.4 45° Flow Field

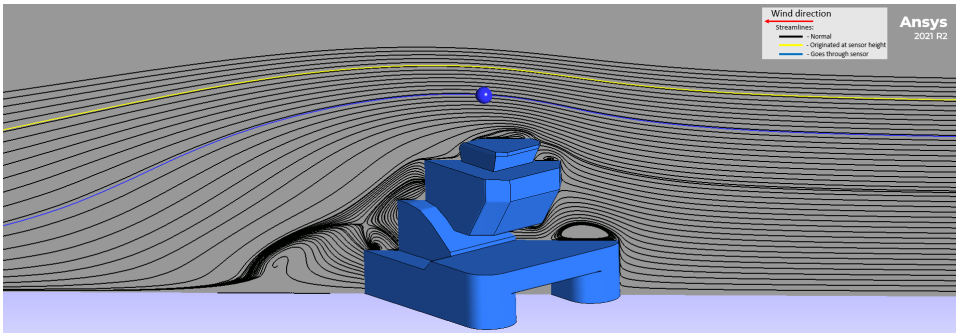

(a) 45° 5 m/s.

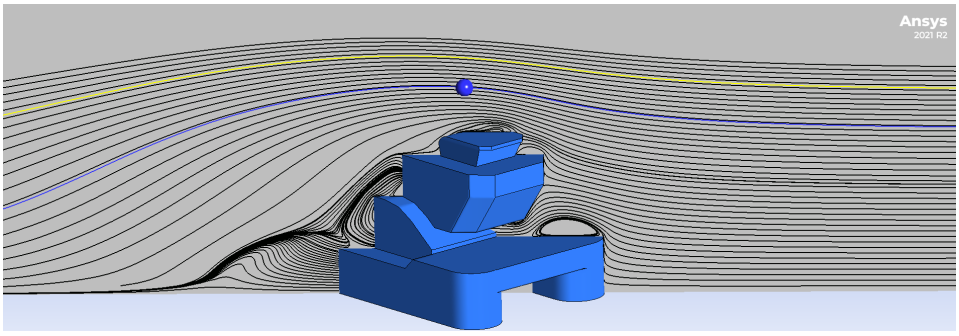

(b) 45° 30 m/s.

Figure 5.6: Streamline plots for the 45° wind angle at wind speeds of 5 m/s and 30 m/s. The blue dot represents the wind sensor. The blue streamline goes through the wind sensor, and the yellow streamline is the one that originated at the sensor height of 12.20 m at the inlet.

The resulting streamline plots for 5 m/s and 30 m/s at the 45° wind angle are shown in Figure 5.6. Both plots look similar, especially on the windward side. The leeward sides are almost identical, except for a small vortex at the edge of the hull in the 5 m/s case, which is not present in the 30 m/s case. Overall, the streamline plots show strong evidence that the flow field is Reynold's number independent, especially near the sensor. The blue streamline originated at a height of 9.94 m, with a wind speed of 4.86 m/s in the 5.00 m/s case.

5.2.5 135° Flow Field

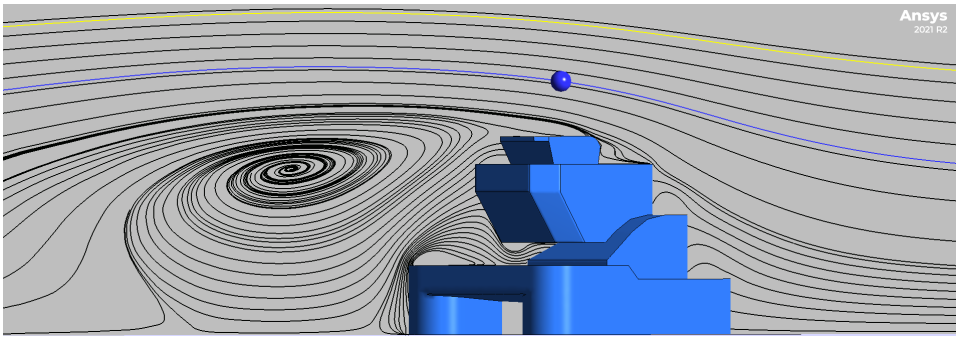

(a) 135° 5 m/s.

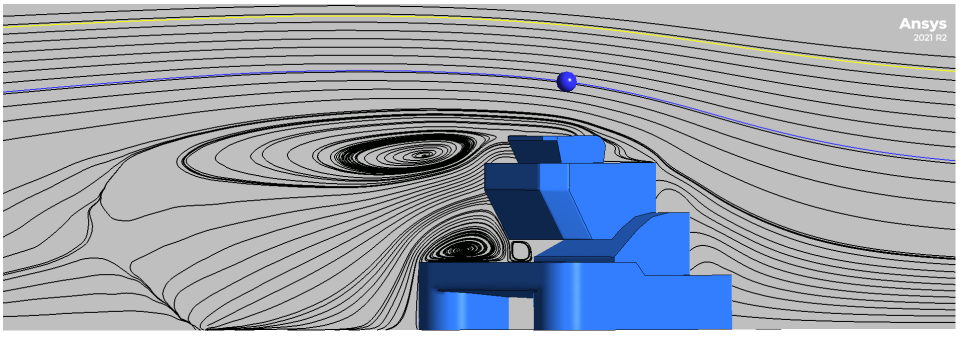

(b) 135° 15 m/s.

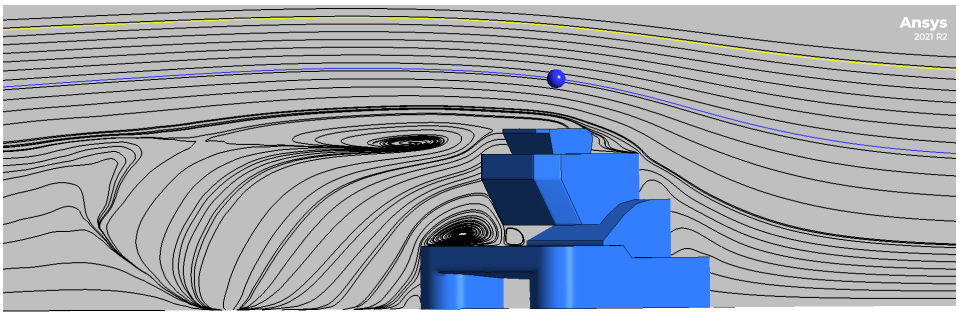

(c) 135° 15 m/s.

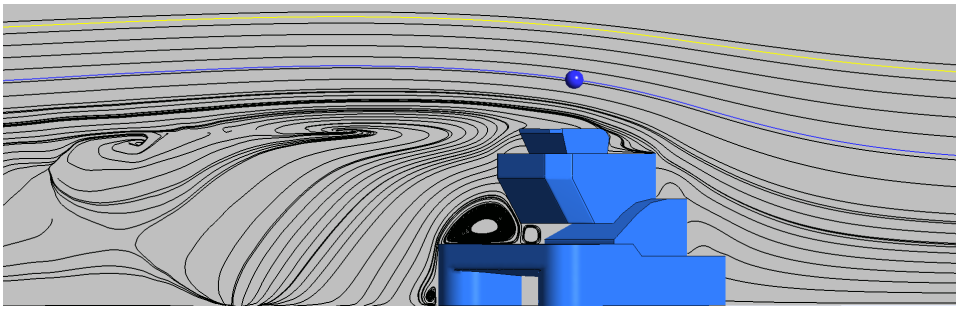

(d) 135° 25 m/s.

Figure 5.7: Streamline plots for the 135° wind angle at wind speeds of 5 m/s and 25 m/s. The blue dot represents the wind sensor. The blue streamline goes through the wind sensor, and the yellow streamline is the one that originated at the sensor height of 12.20 m at the inlet.

The streamline plots of the 135° wind angle are presented in Figure 5.7 for speeds of 5 m/s, 15 m/s, 20 m/s and 25 m/s. The flow structure in the wake is different for all speeds, but the approaching flow and the area around the sensor are the same. Moreover, the streamlines on the leeward side of the ship become increasingly jagged with speed. It is unclear why this occurred; it could be caused by the mesh or by the method Ansys Fluent uses to determine streamlines. Further investigation was not possible within the time constraints.

Nevertheless, the jagged streamlines are confined to the leftmost part of the wake, and the streamlines through the sensor appear to be unaffected. The blue streamline originates at the height of 7.72 m, which corresponds to a speed of 4.69 m/s in the 5.00 m/s case.

5.3 Predicted Velocity Vector at the Sensor

This section presents the numerically predicted velocity components at the sensor location. They will be presented for each incoming wind angle and at all the speeds that were simulated successfully. Missing data are estimated with a trend line. The numerically predicted velocity vector $\boldsymbol{u_{pred}}$ is illustrated in Figure 5.8. The predicted horizontal and vertical wind angles are defined as θ_{pred} and γ_{pred}, respectively.

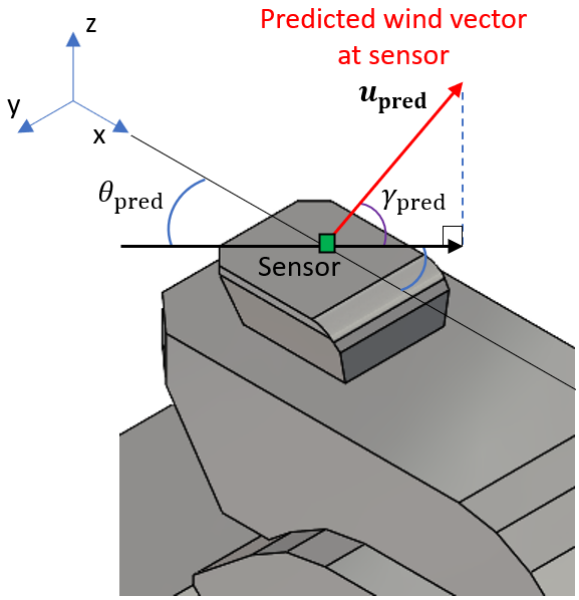

Figure 5.8: Schematic drawing of the numerically predicted wind vector $\boldsymbol{u_{pred}}$ at the sensor. Note that the sensor is merely illustrative and is not drawn at its real location. The angles θ_{pred} and γ_{pred} are the predicted horizontal and vertical wind angles, respectively.

5.3.1 Headwind Velocity Vector

The analysis of the flow fields in the previous section indicated that the headwind flow might be Reynold's number independent. The predicted velocity components at the instrument location, presented in Figure 5.9, lend further credence to this presumption. The figure shows that the relations between the velocity components and the incoming flow speed closely approximate a linear trendline, resulting in high R^2 values of 99.99%, 99.99%, 97.35%, and 99.36% for the magnitude, and the u, v and w components, respectively. These linear relations imply that a change in the incoming flow speed leads to a proportional change in all the velocity components. As a result, a change in the incoming flow speed does not change the direction of $\boldsymbol{u_{pred}}$, only its magnitude. Thus, the headwind flow field is indeed Reynold's number independent.

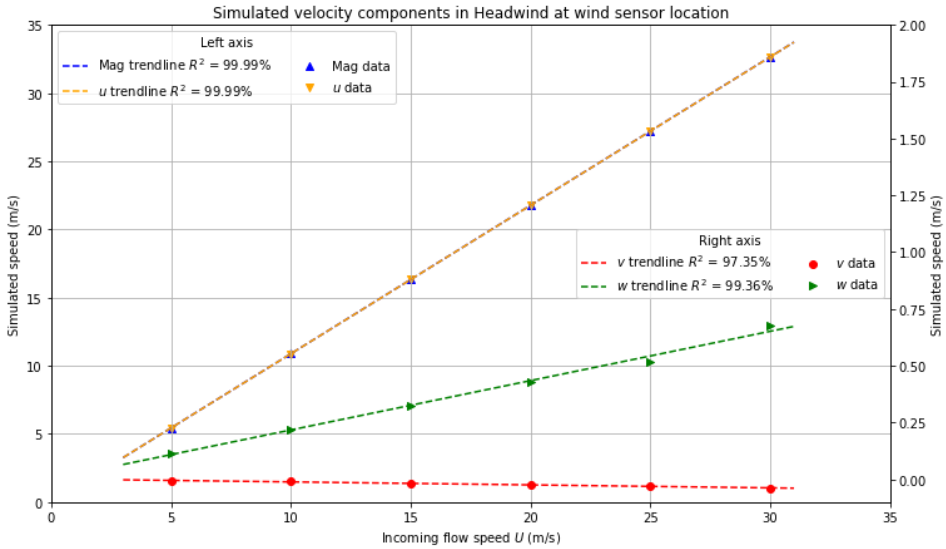

Figure 5.9: Velocity components at the sensor location in headwind for different wind speeds. Includes a second axis for the v and w components.

Furthermore, note that the u component is nearly identical to the magnitude in Figure 5.9. The v and w components have an almost negligible effect on the flow; thus, $\boldsymbol{u_{pred}}$ is expected to be almost horizontal and nearly perfectly parallel to the longitudinal (x) axis, just like the undisturbed wind. Both statements were confirmed by determining the orientation of the predicted velocity vector. The vector has a γ_{pred} of 1.15° and θ_{pred} of -0.06°. The latter angle is minimal and likely beyond the accuracy of this simulation. Thus it is assumed that $\boldsymbol{u_{pred}}$ is perfectly longitudinal.

5.3.2 90° Velocity Vector

Unlike the headwind case, the streamline plots of the 90° wind angle (Figure 5.4) show that the structure of the flow field does change with wind speed. However, this does not appear to be the case for the flow field around the sensor, which suggests that the flow in this area may be locally Reynold's independent.

Figure 5.10 shows the components of $\boldsymbol{u_{pred}}$ for the smallest three incoming wind speeds: 5 m/s, 10 m/s and 15 m/s. Within this range, all the velocity components can be approximated with a linear trendline. The R^2 values for all the components are greater than 98%; thus, the linear approximation matches the data very well. This confirms that the flow field near the sensor is Reynold's number independent for wind speeds between 5 m/s and 15 m/s. It is assumed that this linear trend is maintained over the entire range of wind speeds, up to 30 m/s, in which case the Reynold's number independence extends over the entire range as well.

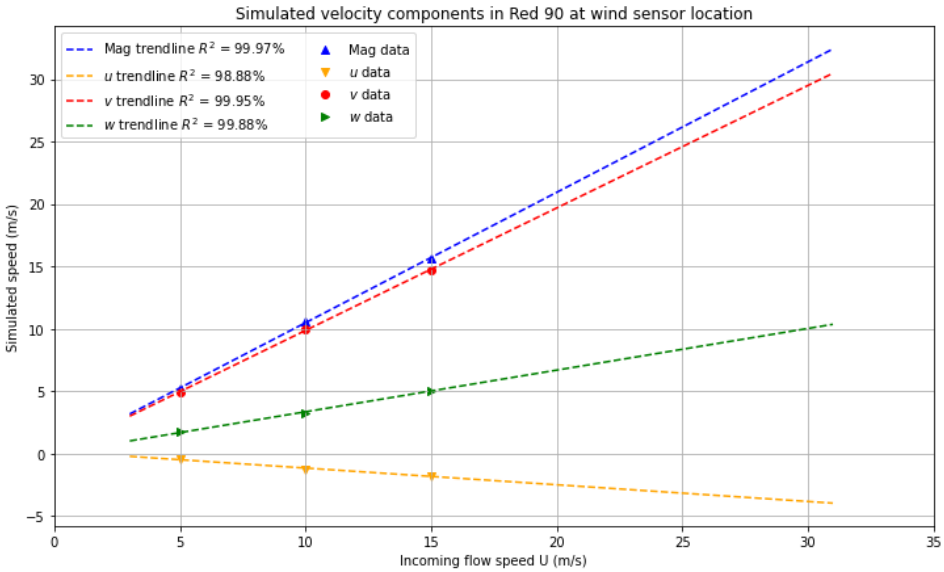

Figure 5.10: Velocity components at the sensor location in 90° wind for different wind speeds.

The undisturbed wind vector is horizontal and approaches the ship at a 90° angle. Therefore, v is the only non-zero component of the undisturbed wind vector. However, Figure 5.10 shows that none of the components of $\boldsymbol{u_{pred}}$ is negligible, which implies that the direction of $\boldsymbol{u_{pred}}$ is different from the undisturbed velocity. The w component of $\boldsymbol{u_{pred}}$ is quite large, resulting in the upward direction of the blue streamline near the sensor in Figure 5.4. Even though the v component is dominant, the negative u component slightly orients $\boldsymbol{u_{pred}}$ towards the bow. The angles θ_{pred} and γ_{pred} were determined to be 96.50° and 18.01°, respectively.

5.3.3 Tailwind Velocity Vector

Figure 5.11 shows the velocity components of $\boldsymbol{u_{pred}}$ for the tailwind case. This plot is similar to the headwind version, with the main difference being the sign of the u component. The v and w components are likewise small. The variation of the velocity components with the incoming wind speed is approximately linear, with R^2 values all greater than 98%. This implies that the flow near the sensor is independent of Reynold's number. This is supported by the streamlines in Figure 5.5, which show that the flow field near the sensor does not change with wind speed. It is assumed that this Reynold's number independence extends over the entire range of wind speeds, from 5 m/s to 30 m/s. Therefore, the direction of $\boldsymbol{u_{pred}}$ does not change with wind speed. γ_{pred} was determined to be 1.49°and θ_{pred} was found to be 180.00°.

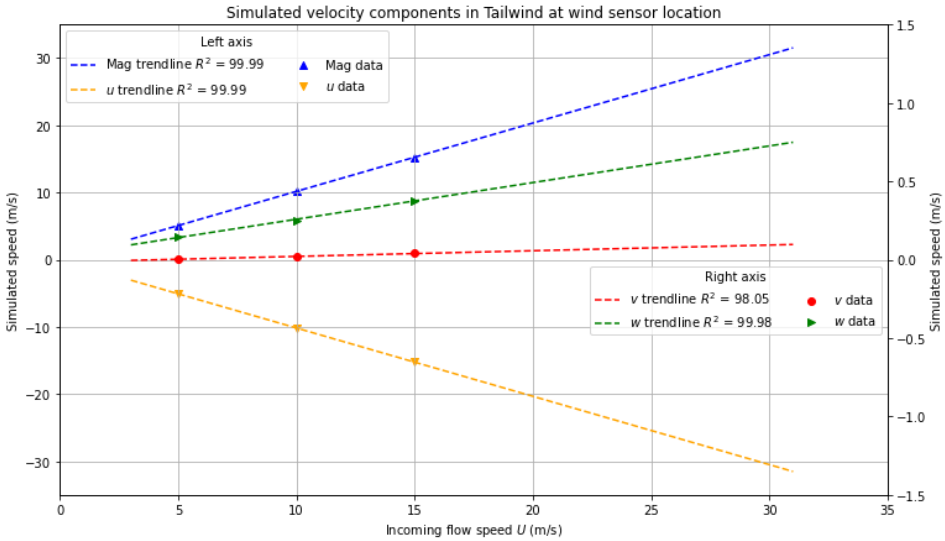

Figure 5.11: Velocity components at the sensor location in tailwind for different wind speeds. Includes a second axis for the v and w components.

5.3.4 45° Velocity Vector

The flow field resulting from a 45° wind angle (Figure 5.6) showed strong signs of being Reynold's number independent, which is confirmed by the predicted velocity components of $\boldsymbol{u_{pred}}$ in Figure 5.12. The variation of all the components with wind speed can be approximated by a linear trendline, with high R^2 values no lower than 99%. The v component of $\boldsymbol{u_{pred}}$ is larger than the u component, resulting in a θ_{pred} of 54.54°. Lastly, γ_{pred} is 3.10°.

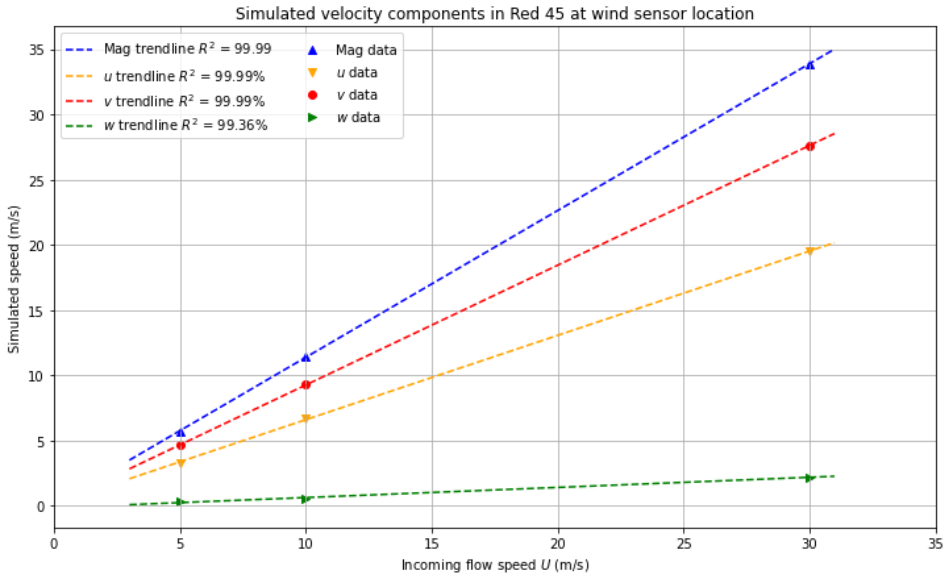

Figure 5.12: Velocity components at the sensor location in 45° wind for different wind speeds.

5.3.5 135°

The predicted velocity components for the 135° wind angle are shown in Figure 5.13. The relationships between the velocity components and the incoming flow speed are close to linear, with R^2 values that are all higher than 99%. This implies that the flow field near the sensor is independent of Reynold's number. This confirms that the effect of the jagged streamlines in Figure 5.7 is not experienced near the sensor. The v component is always larger than the absolute value of the u component, which results in a θ_{pred} of 128.04°. γ_{pred} is 8.19°.

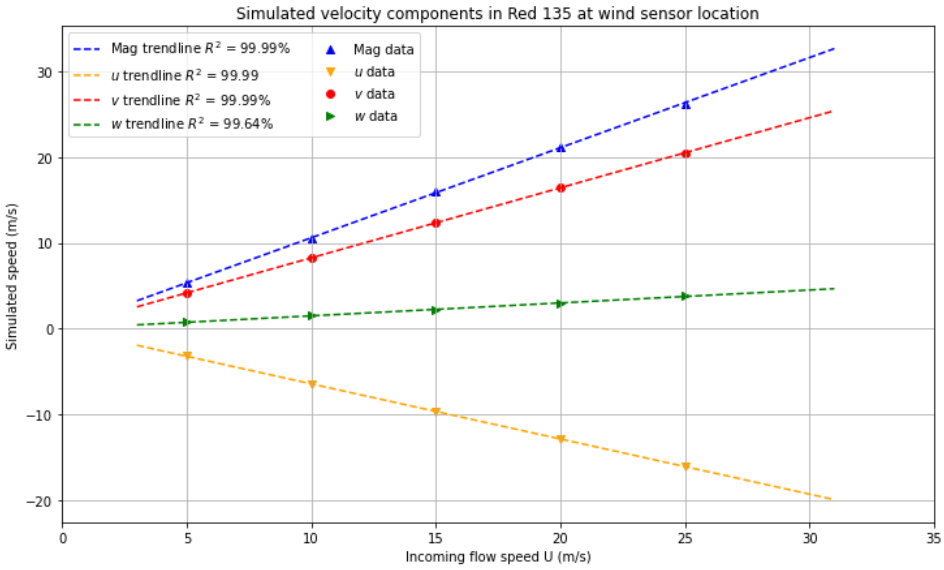

Figure 5.13: Velocity components at the sensor location in 135° wind for different wind speeds.

5.3.6 Slopes of Velocity Components

The slopes of the trendlines of the velocity components and the magnitude in the graphs above are tabulated in Table 5.2. The last row in the table contains the Magnitude Coefficient C_{mag}, which is the inverse of the slope of the magnitude curve:

$$C_{\text{mag}} = \frac{1}{\text{magnitude}} \tag{5.1}$$

Table 5.2: Slopes of the variation of the velocity components with flow speed for all wind angles.

Component (m/s)	**Headwind**	**45°**	**90°**	**135°**	**Tailwind**
Magnitude slope	1.09	1.13	1.05	1.05	1.02
u slope	1.09	0.65	-0.13	-0.64	-1.02
v slope	0.00	0.92	0.98	0.82	0.00
w slope	0.02	0.08	0.33	0.15	0.02
C_{mag}	0.92	0.89	0.96	0.95	0.98

5.4 Measurement Correction Method

In this section, the word "predicted" refers to the **numerically predicted** wind at the sensor location, while the word "measured" refers to the **real** measurement by the sensor **on MS Bard**. The word "true" refers to the **real** incoming wind that a sensor **in isolation** would measure.

The predicted vector directions and magnitude coefficients determined in the previous section are summarised in Table 5.3. Here θ_{pred} is the predicted horizontal wind angle, and θ_{true} is the true horizontal wind angle. γ_{pred} is the predicted vertical wind angle. The 45°, 90° and 135° results have been mirrored to the other side of the ship. Note that all incoming wind is assumed to flow horizontally, making the vertical wind angles irrelevant to the correction process. With the data in Table 5.3, a correction method can be created that inputs the measured wind vector and outputs the true wind vector.

Table 5.3: Predicted vector angles and magnitude coefficients at the sensor location for each true horizontal wind angle.

$\boldsymbol{\theta_{\mathrm{true}}}$	$\boldsymbol{C_{\mathrm{mag}}}$	$\boldsymbol{\theta_{\mathrm{pred}}}$	$\boldsymbol{\gamma_{\mathrm{pred}}}$
0°	0.92	0.00°	1.15°
45°	0.89	54.54°	3.10°
90°	0.96	96.50°	18.01°
135°	0.95	128.04°	8.19°
180°	0.98	180.00°	1.49°
225°	0.95	231.96°	8.19°
270°	0.96	263.50°	18.01°
315°	0.89	305.46°	3.10°

5.4.1 Determination of the True Wind Vector

The true horizontal wind angle can be determined by finding a relation between θ_{true} and θ_{pred}. This relation can then be used to calculate θ_{true} from the measured horizontal wind angle. Next, if a relation between θ_{true} and C_{mag} can be found, then the true wind speed U_{true} can be calculated by multiplying the measured wind speed U_{meas} by the magnitude coefficient that is associated with this particular θ_{true}. With both the true wind speed and true wind angle known, the entire true wind vector is defined.

θ_{true} and θ_{pred} are plotted against each other in Figure 5.14. The plot includes the mirrored data and shows the trend-line that best approximates the provided data and its associated R^2 value.

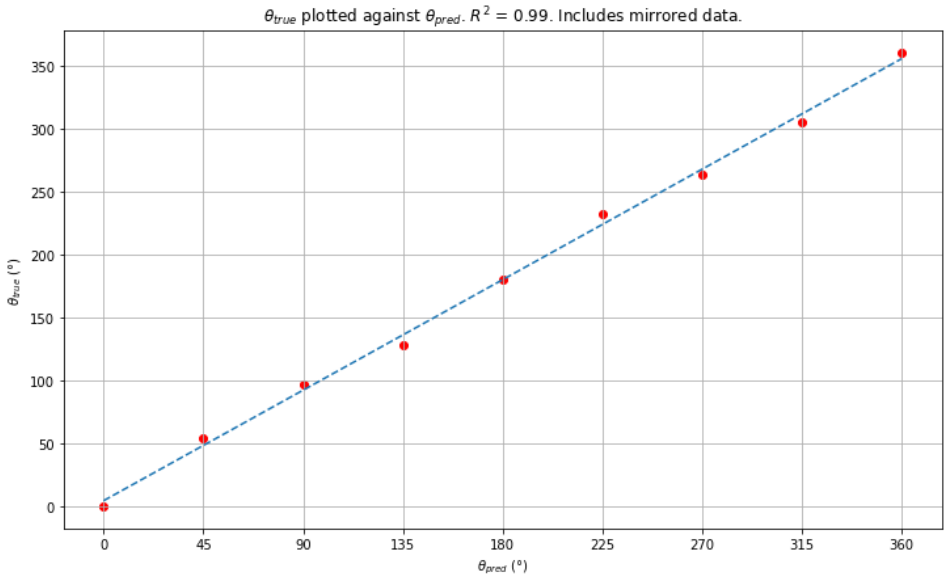

Figure 5.14: Predicted horizontal wind angle θ_{pred} plotted against the true horizontal wind angle θ_{true}. Includes the mirrored data and a linear trend-line.

The data in Figure 5.14 fits a linear trend-line with a very high R^2 value of 0.99. Thus, the true horizontal wind angle can be calculated from the measured horizontal wind angle θ_{meas} with the following equation:

$$\theta_{\mathrm{true}} = 0.9744\theta_{\mathrm{meas}} + 4.6 \tag{5.2}$$

The last thing that needs to be determined to complete the true wind vector is the wind speed. If a relation between θ_{true} and C_{mag} can be found, the true wind speed U_{true} can simply be calculated by multiplying the measured wind speed with the C_{mag} value associated with previously determined θ_{true}. In Figure 5.15, C_{mag} is plotted against θ_{true}.

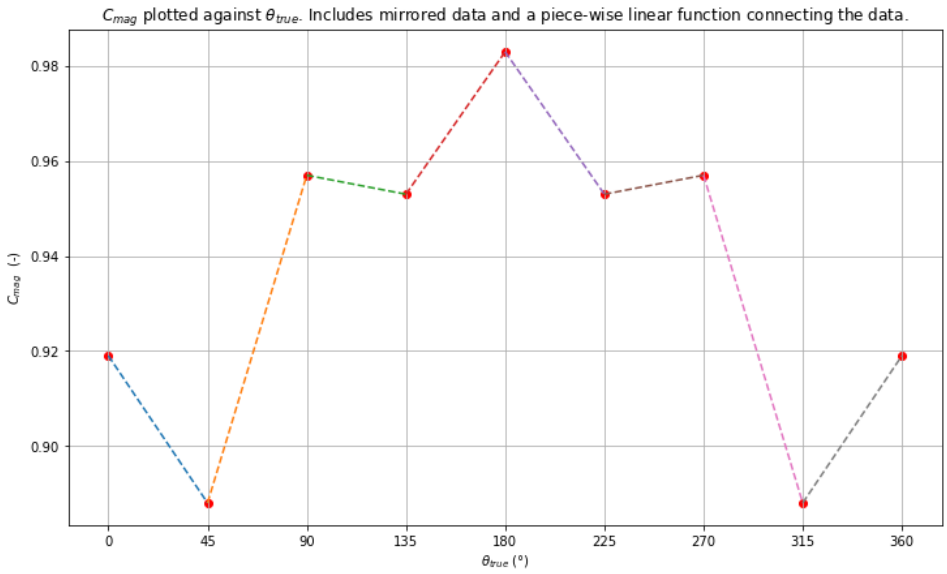

Figure 5.15: Magnitude coefficient C_{mag} plotted against the true horizontal incidence angle θ_{true}. Includes a piece-wise linear function connecting the data.

Figure 5.15 shows that there seems to be no continuous mathematical relation between C_{mag} and θ_{true}. Thus, a piece-wise linear function is used to connect the data points. Note that this assumes that the relation between the data is linear, which is likely not the case for a natural phenomenon. However, using a piece-wise non-linear relation would imply even more assumptions. Therefore, the linear approximation was deemed the best compromise. The piece-wise linear function is presented in Equation 5.3.

$$C_{\text{mag}} = \begin{cases} (-6.89 \cdot 10^{-4}) \cdot \theta_{\text{true}} + 0.919 & 0° \leq \theta_{\text{true}} \leq 45° \\ (1.53 \cdot 10^{-3}) \cdot \theta_{\text{true}} + 0.888 & 45° \leq \theta_{\text{true}} \leq 90° \\ (-8.89 \cdot 10^{-5}) \cdot \theta_{\text{true}} + 0.957 & 90° \leq \theta_{\text{true}} \leq 135° \\ (6.67 \cdot 10^{-4}) \cdot \theta_{\text{true}} + 0.953 & 180° \leq \theta_{\text{true}} \leq 225° \\ (-6.67 \cdot 10^{-4}) \cdot \theta_{\text{true}} + 0.983 & 225° \leq \theta_{\text{true}} \leq 270° \\ (8.89 \cdot 10^{-5}) \cdot \theta_{\text{true}} + 0.953 & 225° \leq \theta_{\text{true}} \leq 270° \\ (-1.53 \cdot 10^{-3}) \cdot \theta_{\text{true}} + 0.957 & 270° \leq \theta_{\text{true}} \leq 315° \\ (6.89 \cdot 10^{-4}) \cdot \theta_{\text{true}} + 0.888 & 315° \leq \theta_{\text{true}} \leq 360° \end{cases} \tag{5.3}$$

5.4.2 Summary of Correction Method

This subsection summarises the process of correcting the wind sensor output for flow distortion by MS Bard. The sensor output consists of the measured horizontal wind direction θ_{meas} and speed U_{meas}. The first step is to convert θ_{meas} to the true horizontal wind direction θ_{true} with the following equation:

$$\theta_{\text{true}} = 0.9744\theta_{\text{meas}} + 4.6 \tag{5.4}$$

With θ_{true} known, the next step is to determine the magnitude coefficient C_{mag}, using the piece-wise linear function presented below. Which expression to use depends on the angular range in which θ_{true} is located.

$$C_{\text{mag}} = \begin{cases} (-6.89 \cdot 10^{-4}) \cdot \theta_{\text{true}} + 0.919 & 0° \leq \theta_{\text{true}} \leq 45° \\ (1.53 \cdot 10^{-3}) \cdot \theta_{\text{true}} + 0.888 & 45° \leq \theta_{\text{true}} \leq 90° \\ (-8.89 \cdot 10^{-5}) \cdot \theta_{\text{true}} + 0.957 & 90° \leq \theta_{\text{true}} \leq 135° \\ (6.67 \cdot 10^{-4}) \cdot \theta_{\text{true}} + 0.953 & 180° \leq \theta_{\text{true}} \leq 225° \\ (-6.67 \cdot 10^{-4}) \cdot \theta_{\text{true}} + 0.983 & 225° \leq \theta_{\text{true}} \leq 270° \\ (8.89 \cdot 10^{-5}) \cdot \theta_{\text{true}} + 0.953 & 225° \leq \theta_{\text{true}} \leq 270° \\ (-1.53 \cdot 10^{-3}) \cdot \theta_{\text{true}} + 0.957 & 270° \leq \theta_{\text{true}} \leq 315° \\ (6.89 \cdot 10^{-4}) \cdot \theta_{\text{true}} + 0.888 & 315° \leq \theta_{\text{true}} \leq 360° \end{cases} \tag{5.5}$$

The final step is to calculate the true wind speed U_{true}, by multiplying the measured wind speed U_{meas} with C_{mag}:

$$U_{\text{true}} = C_{\text{mag}} \cdot U_{\text{meas}} \tag{5.6}$$

U_{true} is then the true incoming wind speed at a height of 12.2 m in a power law based wind profile. This concludes the correction process.

Chapter 6

Discussion

This chapter discusses the effect of the main simplifications and assumptions that have been made in the process of creating the correction method. The chapter starts with a justification for the incompressible flow assumption in Section 6.1, followed by a discussion the CAD model simplifications in Section 6.2. Section 6.3 evaluates the effect of the turbulence model selection. Lastly, Section 6.4 and Section 6.5 cover the sensitivity analyses of the sensor location and the α value of the wind profile, respectively.

6.1 Incompressible Flow Assumption

In this project, the air is assumed to be an incompressible fluid, which means its density does not change with pressure [6]. This assumption is generally considered valid when the flow speed is lower than 30% of the speed of sound [6]. The maximum wind speed that is being simulated is 30 m/s. The speed of sound in air decreases with temperature [36], and Svalbard experiences extremely low temperatures because it is in the Arctic. However, even at a temperature of -30°C, the speed of sound is still 313 m/s, assuming the ideal gas assumption applies [36]. This puts the limit for incompressibility at 104 m/s, which is well over the highest wind speed in this project.

6.2 MS Bard CAD model simplifications

Significant simplifications had to be applied to the MS Bard CAD model to perform the simulations, which would, in turn, impact the simulated flow field. The hulls and the superstructure were transformed into simplified blocks with the same overall dimensions. The streamline plots in Section 5.2 suggest that the shape of the hulls and the first storey have little effect on the flow field near the sensor.

The second storey and the bridge appear to impact the w component of the streamlines near the sensor, but the streamline going through the sensor never gets close to the geometry itself. A more complicated shape may generate more local turbulent flow structures, like vortices, but the sensor streamline would probably be too far away to be affected by those. In conclusion, as long as the overall dimensions of the CAD model remain the same, the velocity predicted at the sensor location probably experiences minimal change.

6.3 Selection of Turbulence Model

In Section 4.1 it was concluded that none of the RANS turbulence models was more accurate than the others in the validation, and the Spalart-Allmaras model was chosen, assuming that all three turbulence models would provide similar results. To test this assumption, the headwind and 90° simulations were repeated with the other two turbulence models at a wind speed of 15 m/s.

Figure 6.1 and Figure 6.2 show the resulting streamline plots from all three turbulence models for the headwind and 90° cases, respectively. Note that each turbulence model in the 90° case predicts a different wake structure but a similar flow field near the sensor. On the other hand, in the headwind case, the k-ε model shows less turbulence near the sensor than the k-ω SST and SA models. Nevertheless, all three turbulence models do not predict turbulent structures at the sensor location.

The predicted velocity components at the sensor location are plotted in Figure 6.3 and tabulated in Table 6.1. The predictions from the k-ε model are very close to those of the SA model, while the k-ω SST model deviates slightly more. However, the differences are small enough to consider the assumption valid. The reason that all models predict a similar velocity vector at the sensor is likely the result of its location. It is located quite far from the ship's surface, in a region where the flow field is not very complex. This is confirmed by the streamline plots, which show little turbulence in this area. While each RANS turbulence model uses different methods to solve the closure problem, they are all still solving the same Reynold's Averaged Navier-Stokes equation. The RANS equation can be expected to dominate the predicted flow field in an area with little turbulence. As a result, the differences caused by each turbulence model should be less pronounced.

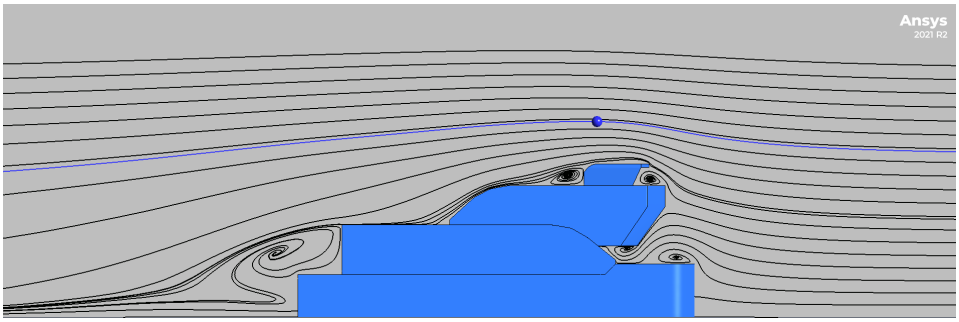

(a) k-ε.

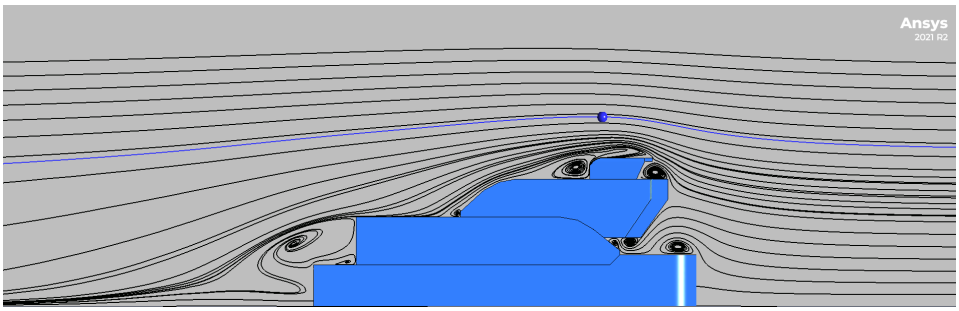

(b) SA.

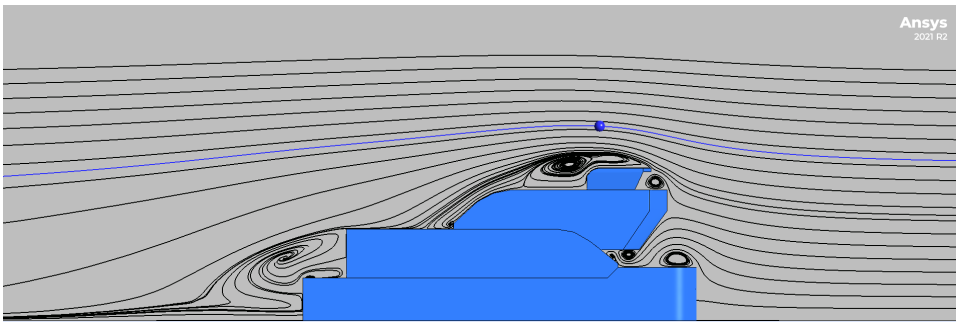

(c) k-ω SST.

Figure 6.1: Streamline plots for the k-ε, Spalart-Allmaras and k-ω SST turbulence models in the headwind, 15 m/s case. The blue dot represents the sensor, and the blue streamline goes through this dot.

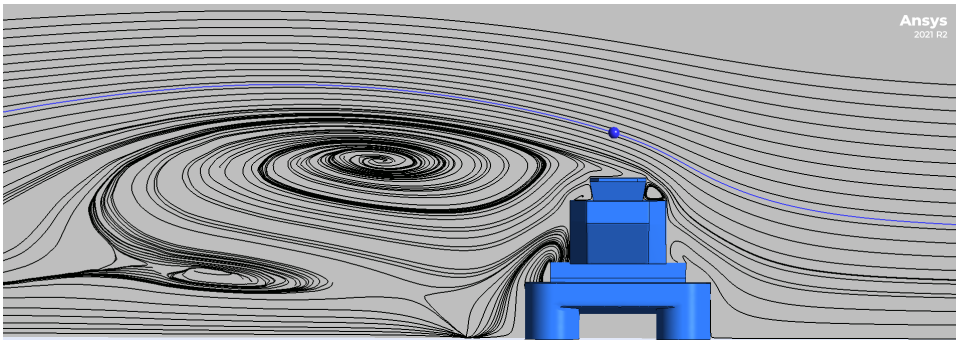

(a) k-ε.

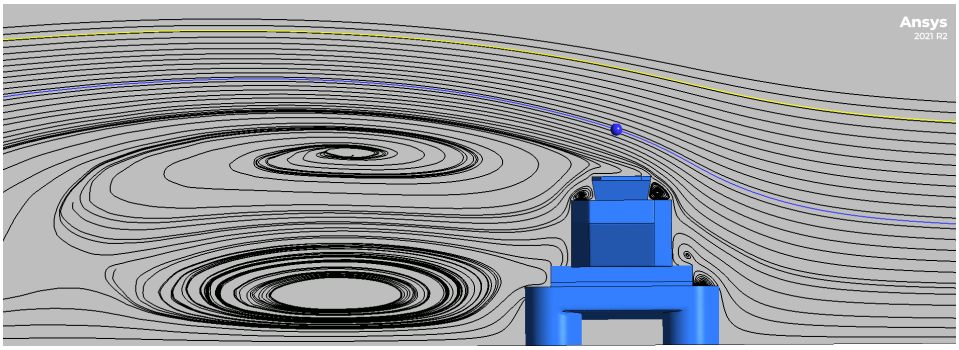

(b) SA.

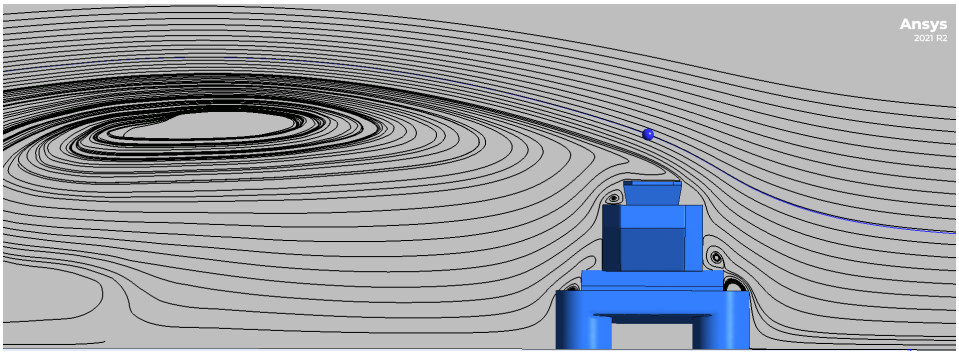

(c) k-ω SST.

Figure 6.2: Streamline plots for the k-ε, Spalart-Allmaras and k-ω SST turbulence models in the 90°, 15 m/s case. The blue dot represents the sensor, and the blue streamline goes through this dot.

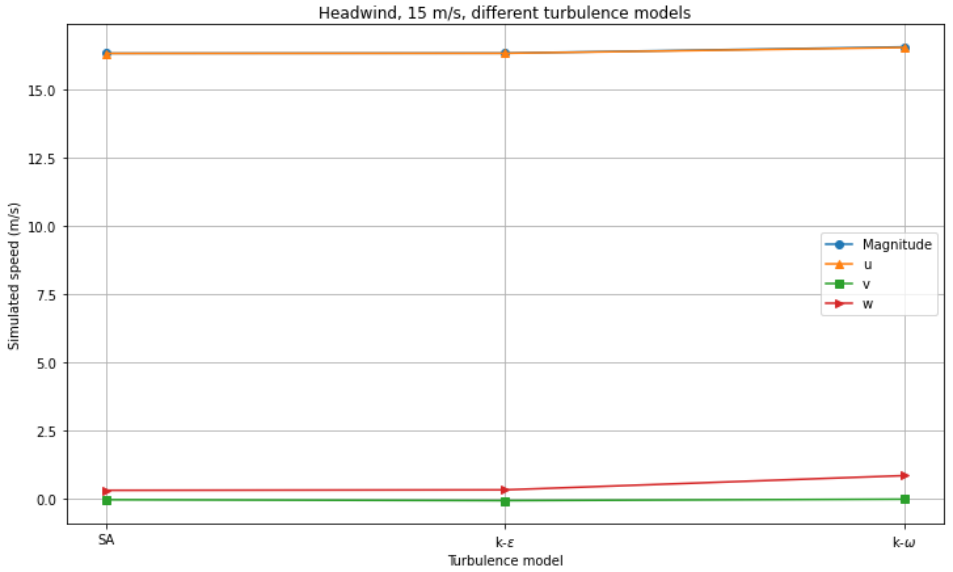

(a) Headwind

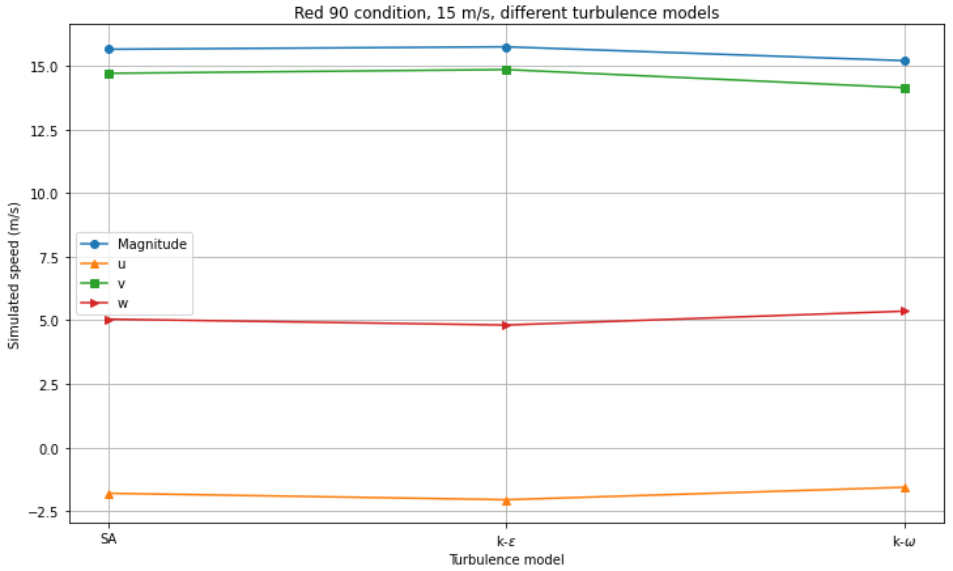

(b) Red 90°

Figure 6.3: Plots showing MS Bard simulation results at the instrument location for all three turbulence models. For the headwind and Red 90° cases.

Table 6.1: Tables presenting MS Bard simulation results at the instrument location for all three turbulence models. For headwind and Red 90° cases.

	Headwind		
	$k-\epsilon$	SA	$k-\omega\ SST$
Magnitude	16.3	16.3	16.6
u	16.3	16.3	16.5
v	-0.05	-0.02	0.00
w	0.34	0.33	0.86

Red 90°		
$k-\epsilon$	SA	$k-\omega\ SST$
15.7	15.6	15.2
-2.05	-1.80	-1.56
14.8	14.7	14.1
4.81	5.04	5.36

6.4 Sensitivity Analysis of Sensor Location

The exact location of the wind sensor on MS Bard was not known prior to this project and had to be measured in situ, with measuring tape. The location of the sensor and the available equipment limited the accuracy of the measurement, resulting in significant error margins. This subsection investigates the effect of this error margin on the accuracy of the correction method.

The wind sensor was determined to be located at the height of 12.20 ± 0.10 m, at 0.27 ± 0.05 m towards the starboard side, and 18.70 ± 0.10 m from the ship's stern. The velocity components at the outer limits of the error margins were acquired for the headwind and 90° cases at 15 m/s. These were then used to evaluate the sensitivity of the simulated flow vector to the sensor location. Table 6.2 gives the coordinates of the limit points where the data was acquired. Each point is given a letter, with which the associated predicted wind speed and horizontal wind angle can be found in Table 6.3.

The last row shows the maximum deviation from the variable at the original sensor location. The maximum angular deviations in both headwind and 90° wind are negligible because they are smaller than the 1° angular resolution of the sensor [31]. The largest deviations in measured wind speed magnitude are 0.04 m/s for headwind and 0.03 m/s for 90° wind, which are higher than the 0.01 m/s sensor resolution. However, the datasheet for the Gill MaxiMet GMX 500 [31] also states that it has an accuracy of ±3% for wind speeds under 40 m/s. Taking the true incoming flow speed of 15 m/s as the reference value, 3% is 0.45 m/s, which is more than 10 times higher than the speed deviation in both cases. Therefore, the speed deviations can be neglected compared to the standard sensor error. In conclusion, it can be safely assumed that the correction method developed in this project is insensitive to the error margin in the sensor location.

Table 6.2: Outer limits of the sensor location measurement error. Each position has a letter that points to the associated data in Table 6.3.

Letter	x-coordinate	y-coordinate	z-coordinate
Original	**-18.7**	**0.27**	**12.2**
A	-18.8	0.27	12.2
B	-18.7	0.27	12.3
C	-18.7	0.22	12.2
D	-18.7	0.27	12.1
E	-18.6	0.27	12.2
F	-18.7	0.32	12.2

Table 6.3: Tables presenting MS Bard simulation results at the instrument location for all three turbulence models. For headwind and 90° cases.

Headwind		
Location	U_{pred} **m/s**	$\theta_{\mathrm{pred}}(^\circ)$
Original	**16.32**	**-0.07**
A	16.34	-0.07
B	16.28	-0.05
C	16.32	-0.04
D	16.37	-0.08
E	16.31	-0.09
F	16.33	-0.10
Max dev.	**0.04**	**0.03**

90°		
Location	U_{pred} **m/s**	$\theta_{\mathrm{pred}}(^\circ)$
Original	**15.65**	**96.5**
A	15.65	97.1
B	15.61	96.9
C	15.63	97.0
D	15.68	97.0
E	15.65	96.9
F	15.66	97.0
Max dev.	**0.03**	**0.6**

6.5 Sensitivity Analysis of Wind Profile

The value of α in the power law model for the atmospheric boundary layer was determined to be 0.14 in Section 4.2.4. However, the determination of this value was arbitrary to some extent. The value of 0.14 was chosen because it was near a value of 0.143 commonly used in engineering and within the 0.11 to 0.14 range suggested by Wang et al. [18]. It was assumed that the exact value of α would not significantly impact the flow field and the correction method.

In order to confirm the validity of this assumption, the 15 m/s eadwind simulation was repeated with two other α values: 0.13 and 0.15. The resulting velocity components predicted at the sensor location are plotted in Figure 6.4 and tabulated in Table 6.4. The plot shows that a small change in the value of α does not significantly change the simulation results at the sensor location. This is affirmed by Table 6.4, which is structured similarly to Table 6.3, and shows that the maximum deviations in U_{pred} and θ_{pred} are smaller than the sensor accuracy determined in the previous section. Thus, the assumption that the value for α in the wind profile has no significant effect on the predicted flow field and the correction method is valid.

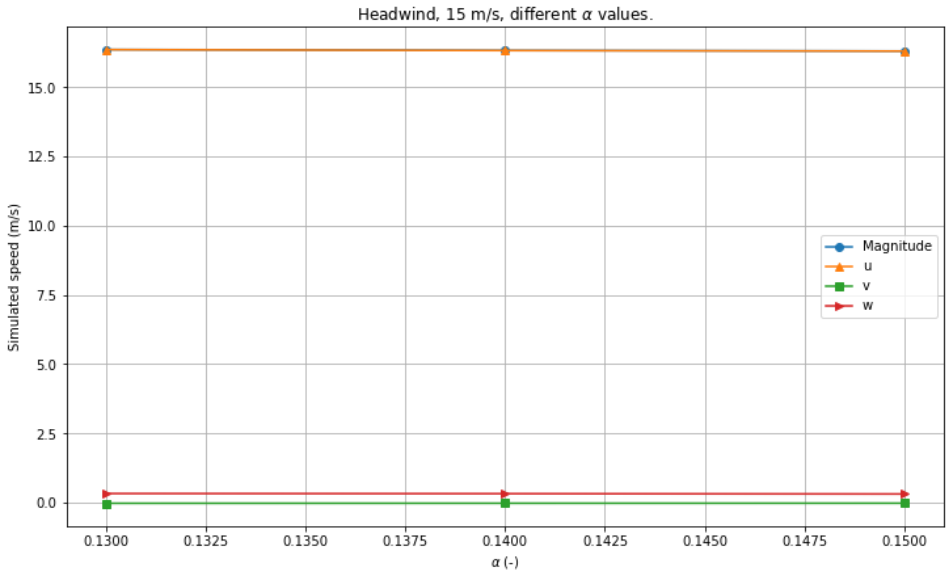

Figure 6.4: Predicted velocity components at the sensor location for different α values: 0.13, 0.14 and 0.15 in the 15 m/s headwind condition.

Table 6.4: Predicted wind speed and horizontal wind angle at the sensor location for different α values: 0.13, 0.14 and 0.15 in the 15 m/s headwind condition.

α	U_{pred}	$\theta_{\mathrm{pred}}(^{\circ})$
0.13	16.36	-0.06
0.14	16.32	-0.07
0.15	16.30	-0.07
Max dev.	**0.03**	**0.00**

Chapter 7

Conclusion

This Master's thesis covered a simulation project on the flow distortion induced by the fjord cruise ship MS Bard on its ship-borne wind sensor measurements. The project was part of the Iwin program by the University Centre in Svalbard.

All simulations in this project were performed with the CFD software Ansys Fluent 2022 R2. The incoming wind was modelled with a power law wind profile, and the flow was assumed incompresssible. The simulation method was validated by using it to recreate the experimental results of Yuan et al. [4] on the Simple Frigate Shape 2. The validation process was also used to determine which RANS turbulence model would be employed for the MS Bard simulations. The turbulence models that were compared were Spalart-Allmaras, k-ε and k-ω SST. The validation results revealed that all three models predicted a similar flow field. In the end, the Spalart-Allmaras turbulence model was selected for the MS Bard simulations.

The MS Bard simulations were performed at wind speeds ranging from 5 m/s to 30 m/s, with 5 m/s intervals, and wind directions ranging from 0° to 180° with 45° intervals. In all the simulations, the streamline plots showed that the flow around the wind sensor was calm, without any turbulent structures. This improved confidence in the results, as RANS models are suitable for these calm turbulent flows. Furthermore, the flow field around the sensor did not change with incoming wind speed for a constant incidence angle. As a result, there is a linear relationship between the incoming wind speed and the predicted velocity components at the sensor location. This was convenient because some of the fluid simulations had diverged, but their results could be accurately estimated using linear regression.

The MS Bard simulation results further confirmed that the choice of the RANS turbulence model had little influence on the flow field predicted near the sensor. Nonetheless, it would change the flow structures in the wake. Additionally, the results were also not sensitive to a change in the α value of the wind profile. However, both the validation and MS

Bard simulation results were grid-dependent, but the error from this was estimated to be negligible compared to the standard error in the wind sensor.

In order to develop the correction method, the port side wind simulation results were mirrored to the starboard side. The relationship between the true wind direction and the predicted wind direction at the sensor location was found to be linear. This linear relation was used to calculate the true wind direction from the wind direction measured by the sensor. No single mathematical expression connected the predicted wind speed data to the true wind speed with a satisfying correlation. Instead, this relation was expressed as a piece-wise linear function. The correction method involves calculating the true wind direction from the measured wind direction with a linear equation and then using the piece-wise function to correct the measured wind speed.

The accuracy of the correction method is difficult to estimate. The primary reason is that there is no experimental data that the simulation results can be compared to. Therefore, it is advised that before employing the correction method, its predictions are compared to the sensor output in a situation where the true wind conditions are available. Additionally, subsequent research on this topic could involve a wind tunnel experiment on a scale model of MS Bard. The results could be used to validate the current correction method or to develop a better one. Moreover, such an experiment would be a valuable addition to the limited amount of research on catamarans. Future studies are also recommended to be carried out over a longer time frame to ensure that CFD meshes can be perfected. This would go a long way in avoiding mesh dependence and the divergence of simulations. Furthermore, more complicated turbulence methods such as unsteady RANS and Large Eddy Simulation could be applied to get a more accurate flow prediction.

Bibliography

[1] UNIS Geophysics Department. Iwin (isfjorden weather information network). https://research.unis.no/iwin/#!team. Accessed on 19-9-2022.

[2] B.I. Moat, M.J. Yelland, R.W. Pascal, and A.F. Molland. An overview of the airflow distortion at anemometer sites on ships. *International Journal of Climatology*, 25: 997–1006, 06 2005.

[3] Hurtigruten Svalbard AS. Ms bard: Hybrid-electric catamaran. https://hurtigrutensvalbard.com/en/about-svalbard/stories-from-svalbard/ms-bard-a-hybrid-electric-catamaran, 2022. Accessed on 18-4-2022.

[4] W. Yuan, A. Wall, and R. Lee. Combined numerical and experimental simulations of unsteady ship airwakes. *Computers & Fluids*, 172:29–53, 8 2018. ISSN 0045-7930.

[5] Australian Government Department of Defence. The technical cooperation program, 2022. Accessed on 24-9-2022.

[6] P.K. Kundu and I.M. Cohen. *Fluid Mechanics*. Elsevier Science Ltd., 2010.

[7] G. B. Arfken, D.F. Griffing, D.C. Kelly, and J. Priest. Chapter 16 - fluid mechanics. In G.B. Arfken, David F. Griffing, Donald C. Kelly, and Joseph Priest, editors, *International Edition University Physics*, pages 306–325. Academic Press, 1984.

[8] D.F. Elger, B.A. Lebret, C.T. Crowe, and J.A. Roberson. *Engineering Fluid Mechanics*. John Wiley & Sons, 11 edition, 2016.

[9] E. Trivyza and E. Boulougouris. Aerodynamic study of superstructures of megayachts. In *9th International Workshop on Ship and Marine Hydrodynamics*, pages 26–28. University of Strathclyde, August 2015.

[10] J. Blazek. *Computational Fluid Dynamics: Principles and Applications*. Elsevier Science Ltd., 1 edition, 2001.

[11] F. M. White. *Fluid Mechanics*. McGraw-Hill, 2002.

[12] J. Bardina, P. Huang, and T. Coakley. Turbulence modeling validation, testing, and development. *NASA Technical Memorandum*, 5 1997.

[13] F.R. Menter. Improved two-equation k-omega turbulence models for aerodynamic flows. *NASA Technical Memorandum*, 10 1992.

[14] S.H. Ko, C. Kim, K.H. Kim, and K.W. Cho. Investigation of turbulence models for multi-stage launch vehicle analysis including base flow. In Ecer A. Satofuka N. Periaux J. Kwon, J.H. and P. Fox, editors, *Parallel Computational Fluid Dynamics 2006*, pages 277–284. Elsevier Science B.V., Amsterdam, 2007.

[15] ANSYS, inc. *ANSYS Fluent User's Guide*. ANSYS, inc, January 2019.

[16] Emil Simiu. *Design of Buildings for Wind - A Guide for ASCE 7-10 Standard Users and Designers of Special Structures (2nd Edition)*. John Wiley & Sons, 2011.

[17] J. Forrest and I. Owen. An investigation of ship airwakes using detached-eddy simulation. *Computers & Fluids*, 39:656–673, 04 2010.

[18] P. Wang, F. Wang, and Z. Chen. Investigation on aerodynamic performance of luxury cruise ship. *Ocean Engineering*, 213, 10 2020. ISSN 00298018.

[19] J.S. Touma. Dependence of the wind profile power law on stability for various locations. *Journal of the Air Pollution Control Association*, 27(9):863–866, 1977. doi: 10.1080/00022470.1977.10470503.

[20] J. S. Forrest, C. H. Kaaria, and I. Owen. Evaluating ship superstructure aerodynamics for maritime helicopter operations through cfd and flight simulation. *Aeronautical Journal*, 120:1578–1603, 10 2016. ISSN 00019240.

[21] C. Kääriä, J. Forrest, I. Owen, and G.D. Padfield. Simulated aerodynamic loading of an sh-60b helicopter in a ship's airwake development, validation and integration of carrier air-wake simulations for use in fixed-wing and rotary-wing flight simulation view project horizontal axis tidal stream turbines subject to wave-current interaction view project, 09 2009.

[22] Shi Y.J. Su, D.C. and G.H. Xu. Numerical study of the rotational direction effect on aerodynamic loading characteristics of shipborne helicopter rotor. *The Aeronautical Journal*, 123(1263):635–657, 2019.

[23] H.C. Lim, I.P. Castro, and R.P. Hoxey. Bluff bodies in deep turbulent boundary layers: Reynolds-number issues. *Journal of Fluid Mechanics*, 571:97–118, 2007.

[24] G.L. Larose and A. D'Auteuil. On the reynolds number sensitivity of the aerodynamics of bluff bodies with sharp edges. *Journal of Wind Engineering and Industrial Aerodynamics*, 94(5):365–376, 2006. ISSN 0167-6105. The eighth Italian National Conference on Wind Engineering IN-VENTO-2004.

[25] R.P. Hoxey, A.M. Reynolds, G.M. Richardson, A.P. Robertson, and J.L. Short. Observations of reynolds number sensitivity in the separated flow region on a bluff body. *Journal of Wind Engineering and Industrial Aerodynamics*, 73:231–249, 1998.

[26] B.I. Moat, M.J. Yelland, and I.M. Brooks. Airflow distortion at instrument sites on the oden during the acse project. Project report, December 2015.

[27] B.I. Moat and M.J. Yelland. Airflow distortion at instrument sites on the rv knorr. Project report, 1998.

[28] Engineering ToolBox. Air - Dynamic and Kinematic Viscosity, 2003. Accessed on 14-6-2022.

[29] Engineering ToolBox. Air - Density, Specific Weight and Thermal Expansion Coefficient vs. Temperature and Pressure., 2003. Accessed on 14-6-2022.

[30] MarineTraffic – Global Ship Tracking Intelligence (www.marinetraffic.com). Ms bard. Accessed on 4-3-2022.

[31] Gill MaxiMet Ltd. *CMX500 Compact Weather Station*, 2019.

[32] D. J. Sherman, C. Houser, and A. C.W. Baas. Electronic measurement techniques for field experiments in process geomorphology, 2013.

[33] Environmental monitoring of Svalbard and Jan Mayen. Air temperature and precipitation. `https://www.mosj.no/en/climate/atmosphere/temperature-precipitation.html`, March 2022. Accessed on 14-6-2022.

[34] A. Albani and M. Z. Ibrahim. Wind energy potential and power law indexes assessment for selected near-coastal sites in malaysia. *Energies*, 10(3), 2017. ISSN 1996-1073.

[35] H.Y. Wong. A means of controlling bluff body flow separation. *Journal of Wind Engineering and Industrial Aerodynamics*, 4(2):183–201, 1979. ISSN 0167-6105.

[36] N. Hall. Beginner's Guide to Aerodynamics. https://www.grc.nasa.gov/www/k-12/airplane/index.html, May 2021. Accessed on 3-8-2022.